Docket No.: 209774US0PCT

BOARD OF PATENT APPEALS AND INTERFERENCES
ALEXANDRIA, VIRGINIA 22313
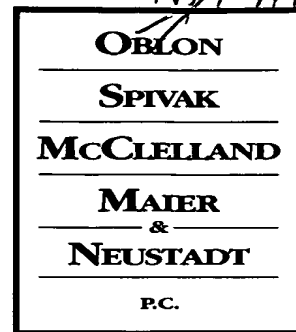
RE: Application Serial No.:   09/869,123
     Applicants: Karsten REIHS, et al.
     Filing Date: October 3, 2001
     For: ULTRAPHOBIC SURFACE
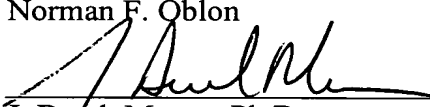   Group Art Unit: 1711

SIR:

Attached hereto for filing are the following papers:

Appeal Brief
Request for Extension of Time (4-months)
References (3)

Our credit card payment form in the amount of **$2,090.00** is attached covering any required fees. In the event any variance exists between the amount enclosed and the Patent Office charges for filing the above-noted documents, including any fees required under 37 C.F.R 1.136 for any necessary Extension of Time to make the filing of the attached documents timely, please charge or credit the difference to our Deposit Account No. 15-0030. Further, if these papers are not considered timely filed, then a petition is hereby made under 37 C.F.R. 1.136 for the necessary extension of time. A duplicate copy of this sheet is enclosed.

Respectfully submitted,

OBLON, SPIVAK, McCLELLAND,
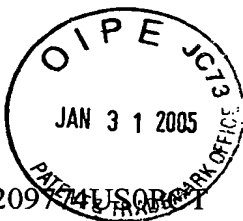MAIER & NEUSTADT, P.C.
Norman F. Oblon

J. Derek Mason, Ph.D.
Registration No. 35,270

Customer Number
22850
(703) 413-3000 (phone)
(703) 413-2220 (fax)

IN THE UNITED STATES PATENT & TRADEMARK OFFICE

IN RE APPLICATION OF   :

KARSTEN REIHS, ET AL.   : EXAMINER:

SERIAL NO: 09/869,123   :

FILED: OCTOBER 3, 2001   : GROUP ART UNIT: 1711

FOR: ULTRAPHOBIC SURFACE   :

APPEAL BRIEF

BOARD OF PATENT APPEALS AND INTERFERENCES
ALEXANDRIA, VIRGINIA 22313

SIR:

This is an appeal of Claims 1-10, 27, 28 and 52-54, which were finally rejected in the

Official Action dated January 29, 2004. A Notice of Appeal was timely filed on July 29,

2004.

I. REAL PARTIES OF INTEREST

The real party of interest in this appeal is: Sunyx Surface Nanotechnologies GmbH,

Stolberger Str. 370, D-50933, Koeln, Federal Republic of Germany.

II. RELATED APPEALS AND INTERFERENCES

Appellants, Appellants' legal representative, and the Assignees are aware of no other

appeals or interferences which will directly affect or be directly affected by or have a bearing

on the Board's decisions in this appeal.

III. STATUS OF THE CLAIMS

Claims 1-10, 27, 28 and 52-54 are active and under Final Rejection in the present application. Claims 11-26 and 29-51 stand withdrawn.

IV. STATUS OF AMENDMENTS

All previously filed amendments have been entered.

V. SUMMARY OF THE INVENTION

The present invention relates to a surface having ultraphobic properties, which comprises a hydrophobic or oleophobic material, or is coated by a hydrophobic or oleophobic material, and has a surface topography in which the value of the integral of a function S

$$S(\log f) = a(f) \cdot f$$

which gives a relationship between the spatial frequencies f of the individual Fourier components and their amplitudes a(f), and wherein the value of the integral is at least 0.5 between the integration limits $\log(f_1/\mu m^{-1}) = -3$ and $\log(f_2/\mu m^{-1}) = 3$. (see page 1, lines 3-12; page 2, line 29 to page 3 line 6; claim 1)

Appellants have found that by providing such surfaces having the required value of at least 0.5 for the integral of function S within the stated limits, one method for obtaining an ultraphobic surface is obtained.

An ultraphobic surface is characterized by the fact that the contact angle of a drop of liquid, usually water, on the surface is significantly more than 90° and the roll-off angle does not exceed 10°. Ultraphobic surfaces with a contact angle of >150° and the above noted roll-off angle are industrially very useful, since they are wettable neither with oil nor water, soil particles adhere to the surfaces very poorly and the surfaces are self-cleaning. (see specification at page 1, lines 14-21).

2

VI. ISSUES

The issues in this appeal are:

1. Whether the claims are anticipated under 35 U.S.C. 102(b) or obvious under 35

   U.S.C. 103 over Clark et al or Takahashi et al, alone or in view of either of

   Baumann et al or Goetz et al?

2. Whether the Declarations filed by Dr. Reihs under 37 C.F.R. 1.132 are sufficient

   to show that the claims are not anticipated or obvious in light of any of the cited

   references?

3. Whether the specification is enabling for the claims as pending, under 35 U.S.C.

   112, first paragraph?

VII. GROUPING OF CLAIMS

The claims stand or fall together.

VIII. ARGUMENT

The claims stand rejected, in various combinations, under 35 U.S.C. 102(b) over

Clark et al or Takahashi et al, or under 35 U.S.C. 103(a) over Clark et al in view of Baumann

et al, or Takahashi et al in view of Goetz et al. None of the applied references describe an

ultraphobic surface having the claimed surface topography.

The Examiner's position relies upon the assertion that either Clark or Takahashi

inherently describe a structured surface having the claimed surface topography. The

Examiner's reasoning for this is that because Clark or Takahashi disclose ultraphobic

surfaces having high contact angles above 150°, they inherently must have the surface

topography required in the present claims, even though neither reference discloses or

3

suggests anything with respect to the surface topography as present in the present claims. Accordingly, the Examiner bases the rejections on a theory of inherency. The Examiner's position that any ultraphobic surface having a contact angle above 150° would inherently have a surface topography with the value of S of the claims is traversed and has been amply rebutted by the Declarations of Dr. Reihs filed previously in this application.

The prior Rule 1.132 Declarations show that surfaces described in the prior art, which have contact angles in excess of 150° and provide roll off of water droplets at the "slightest inclination of the substrate" (i.e., Clark at column 6, lines 52-53) do not *necessarily* possess the claimed surface topography. The Declaration shows that although a surface may have ultraphobic properties, it does not necessarily or inherently have the claimed surface topography (i.e., Examples 1, 7, 8, and 10 of Clark). The data of Examples 1, 7, 8 and 10 of the Clark reference (U.S. Patent 5,674,592) were used to calculate the topography of surfaces consisting of nanostructure elements according to Clark as embodied in the S integral value as used in the present invention. In particular, the data used were the height of the nanostructure elements, the tip diameter of the nanostructure elements and the areal number densities of the nanostructure elements. These were the same data used in calculating the value of the S integral in the examples of the present application. The calculations were performed with 262,144 points per calculation. This number of points per calculation is more than adequate to model the topography accurately.

The resulting height profiles were processed in exactly the same manner as described in the present application at page 14, lines 23-27; page 25, lines 1-22 and page 29, lines 6-19, and as described in Dr. Reihs' first Declaration. No manipulation of the data was required or performed in order to calculate the S integral value. The calculations were performed in exactly the same manner as the examples in the present application using exactly the same type of data. The methods used to calculate height profiles using the data discussed above

4

are well known to those of skill in the art and are discussed in detail in the references described in the specification (copies of the Magonov et al, Ruppe et al and Recknagel et al references cited in the specification and incorporated therein by reference are provided for the Board's convenience). From these data (height, tip diameter and areal density of nanostructure elements on the surface) one of ordinary skill readily obtains the height profiles that are used in the present invention for determining the S integral value of the surface.

The number m=n=512 points in both x and y directions was used, since it matches the number of points in the x and y directions of the height profiles in the examples of the present application (see, for example, page 28, line 1 to page 29, line 4). Accordingly this choice of the number of points in each of the x and y directions was chosen to make the results calculated in the examples of the present application and those calculated based upon the data in Clark be directly comparable.

With respect to the hydrophobic substance modeled in the calculations reported in the Declarations: In the Clark patent, the hydrophobic substance $C_8F_{17}(CH_2)_{11}SH$ on smooth gold consists of a contact angle of $\Theta_a = 125°$ (advancing contact angle Θ_a) and $\Theta_r = 105°$ (receding contact angle Θ_r) (see Table 2, example 3 of Clark) Since the contact angle hysteresis $\Delta\Theta = \Theta_a - \Theta_r = 20°$ is small, one can approximate the apparent contact angle Θ (or equilibrium contact angle) according to the well known equation $\Delta\Theta \sin\Theta \approx \cos\Theta_r - \cos\Theta_a$ (see e.g. J. Kijlstra et al, Colloids and Surfaces 206, 521 (2002)) yielding $\Theta = 116°$. The model used in the Declaration thus implies an apparent contact angle of a smooth gold coated surface of $\Theta = 115°$ as seen from example 6 in the specification. Thus the model used in the Declaration corresponds to a hydrophobic coating equivalent to the compound used in the Clark patent.

Accordingly, as shown in Table 1 of the first Reihs Declaration, no additional information was needed beyond the information provided by Clark and the model used in the present invention to carry out the calculations and verify that even though Clark shows a

contact angle larger than 170°, the surfaces provided by Clark do **not** provide a surface structure resulting in an integral S (log f) of at least 0.5, as required in the present invention. The integrals achieved with the surfaces according to Clark ranged from 0.017 to 0.134 and are thus at least three times smaller than the value of the integrals claimed. Accordingly, the structure of the surfaces generated according to Clark are significantly different from the structure of the surfaces of the present invention, even though the structures of Clark have comparable water contact angles.

Appellants therefore respectfully submit that the Declarations are sufficient to show that surfaces having ultraphobic properties do not inherently possess the claim surface topography, and to address the Examiner's concerns.

Thus, there is no basis for the Examiner's conclusion that any ultraphobic surface having a contact angle above 150° would inherently have a surface topography with the value of S of the present claims and, therefore, the claims are not anticipated by the references.

Accordingly, since it has been shown that ultraphobic surface properties do not depend on the claimed surface topography, the Examiner can no longer assert that the claimed surface topography is *inherent* to ultraphobic surfaces. Thus, Appellants' Declaration is sufficient to show that neither Clark nor Takahashi inherently describe the claimed surface topography. Accordingly, since Clark and Takahashi neither expressly nor inherently describe the claimed surface topography, Clark and Takahashi fail to anticipate the claimed surface and the rejections under 35 U.S.C. 102(b) should be REVERSED.

Moreover, because neither Clark nor Takahashi expressly or inherently describe a surface having the claimed topography, as discussed above, the Examiner has failed to support a *prima facie* case of obviousness. None of the applied references in combination with Clark or Takahashi "teach or suggest all the claim limitations" (M.P.E.P. § 21143). The Baumann et al and Goetz et al references are used by the Examiner to merely teach a

particular material used in the substrate, but say nothing about the surface topography required by the present claims. Accordingly, none of the applied references, either individually or in combination suggest the claimed invention, and the rejections under 35 U.S.C. 103 should be REVERSED.

The rejection of the claims under 35 U.S.C. § 112, first paragraph is respectfully traversed. The Examiner states that the specification "does not reasonably provide enablement for *any and every* surface having the claimed properties" (emphasis added). However, Appellants respectfully submit that the Examiner has applied an incorrect legal standard. In *Engel Industries, Inc. v. Lockformer Co.*, the Federal Circuit noted "The enablement requirement is met if the description enables *any* mode of making and using the claimed invention." (emphasis added).[1] While it is true that enablement requires that there be no undue experimentation required, it is well established that the invention can be enabled "even though some experimentation is necessary; the amount of experimentation, however, must not be unduly extensive."[2] M.P.E.P. § 2164.01(b) states that "as long as the specification discloses *at least one method* for making and use the claimed invention that bears a reasonable correlation to the entire scope of the claim, then the enablement requirement if 35 U.S.C. § 112 is satisfied" (emphasis added). In *National Recovery Technologies, Inc. v. Magnetic Separation Systems, Inc.*, the Federal Circuit noted that the "scope of enablement in turn, is that which is disclosed in the specification plus the scope of what would be known to one of ordinary skill in the art without undue experimentation."[3]

The Examiner has already admitted that the specification is "enabling for the product made in the examples in the specification". For that reason alone, Appellants respectfully submit that the claimed invention is sufficiently "enabled" by the specification. Further,

---

[1] *Engel Industries, Inc. v. Lockformer Co.*, 946 F.2d 1528; 20 U.S.P.Q.2d 1300 (Fed. Cir. 1991).
[2] *United States v. Telectronics, Inc.*, 857 F.2d 778, 8 U.S.P.Q.2d 1217 (Fed. Cir. 1988), *cert. denied*, 490 U.S. 1046 (1989).
[3] *National Recovery Technologies, Inc. v. Magnetic Separation Systems, Inc.*, 166 F.3d 1190, 49 U.S.P.Q.2d 1671 (Fed. Cir. 1999).

Appellants have described significantly more than one method of making and using the claimed invention. The Examples of the specification describe various different methods for preparing a surface having the claimed surface topography (e.g., by etching or deposition of fine particles), and provide examples of various oleophobic and hydrophobic materials. Furthermore, the specification provides a detailed description at pages 28-29, of methods for determining surface topography, complete with reference to various published articles describing those methods that were thus clearly known to those of skill in the art.
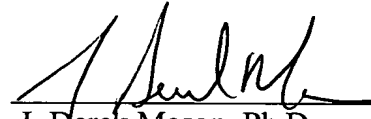
Moreover, Appellants respectfully submit that one of ordinary skill in the art would reasonably understand, based on the ample description and examples of the present specification, how to make and use the claimed invention. While the standard requires that one of ordinary skill must be able to practice the invention without undue experimentation, as noted above, this does not require that each and every embodiment must be explicitly described in the application. Further, this standard does not require that <u>no</u> experimentation be needed to practice the full scope of the invention. Given the disclosure in the present application of methods for making the present ultraphobic surfaces having the required surface topography, the disclosure of a variety of materials for preparing such surfaces, and the method by which to determine whether the formed surfaces have the required topography, one of ordinary skill in the art would be readily able to practice the invention without requiring undue experimentation. Accordingly, Appellants respectfully submit that the claimed invention is enabled, based upon the description in the specification, combined with the knowledge of one of ordinary skill in the art, and lastly as admitted by the Examiner in the statement that Appellants have enabled the examples described in the application.

Appellants respectfully submit that the application is now in condition for allowance,

and that all of the rejections should be REVERSED.

Respectfully submitted,

OBLON, SPIVAK, McCLELLAND,
MAIER & NEUSTADT, P.C.
Norman F. Oblon

J. Derek Mason, Ph.D.
Attorney of Record
Registration No. 35,270

Customer Number
22850

Tel: (703) 413-3000
Fax: (703) 413 -2220
(OSMMN 06/04)

APPENDIX
LISTING OF CLAIMS

Claim 1. (Previously Presented) A surface having ultraphobic properties, comprising a surface topography in which the value of the integral of a function S

$$S(\log f) = a(f) \cdot f \quad (1),$$

which gives a relationship between the spatial frequencies f of the individual Fourier components and their amplitudes a(f), is at least 0.5 between the integration limits $\log(f_1/\mu m^{-1}) = -3$ and $\log(f_2/\mu m^{-1}) = 3$, wherein said surface comprises a hydrophobic or oleophobic material, or is coated with a hydrophobic or oleophobic material.

Claim 2. (Previously Presented) The surface according to Claim 1, wherein the integral is > 0.6.

Claim 3. (Previously Presented) The surface according to Claim 1, wherein said surface has a contact angle of at least 150° and a roll-off angle of <10°.

Claim 4. (Previously Presented) The surface according to Claim 1, wherein said surface has a contact angle of at least 155°.

Claim 5. (Previously Presented) The surface according to Claim 1, wherein said surface comprises metal, plastic, glass or ceramic.

Claim 6. (Previously Presented) The surface according to Claim 1, wherein said surface comprises metal and is selected from the group consisting of beryllium, magnesium, scandium, titanium, vanadium, chromium, manganese, iron, cobalt, nickel, copper, zinc, aluminum, gallium, yttrium, zirconium, niobium, molybdenum, technetium, ruthenium, rhenium, palladium, silver, cadmium, indium, tin, lanthanum, cerium, praseodymium, neodymium, samarium, europium, gadolinium, terbium, dysprosium, holmium, erbium, thulium, ytterbium, lutetium, hafnium, tantalum, tungsten, rhenium, osmium, iridium, platinum, gold, thallium, lead, bismuth, titanium, aluminium, magnesium, nickel and alloys thereof.

Claim 7. (Previously Presented) The surface according to Claim 1, wherein said surface comprises metal and is an aluminium-magnesium alloy.

Claim 8. (Previously Presented) The surface according to Claim 1, wherein said surface comprises plastic and is a thermosetting or thermoplastic polymer.

Claim 9. (Previously Presented) The surface according to Claim 1, wherein said surface comprises a thermosetting polymer and is selected from the group consisting of diallyl phthalate resins, epoxy resins, urea-formaldehyde resin, melamine-formaldehyde resin, melamine-phenol-formaldehyde resin, phenol-formaldehyde resin, polyimides, silicone rubbers, unsaturated polyester resins and mixtures thereof.

Claim 10. (Previously Presented) The surface according to Claim 1, wherein said surface comprises a coating of a hydrophobic phobicization auxiliary.

Claim 11. (Withdrawn) Material or construction material comprising an ultraphobic surface according to Claim 1.

Claim 12. (Withdrawn) A friction-reducing lining of vehicle bodies, aircraft fuselages or hulls of ships comprising the ultraphobic surface as claimed in claim 1.

Claim 13. (Withdrawn) A self-cleaning coating or panelling of building structures, roofs, windows, ceramic construction material comprising the ultraphobic surface claimed in Claim 1.

Claim 14. (Withdrawn) An antirust coating of metal objects comprising the ultraphobic surface claimed in Claim 1.

Claim 15. (Withdrawn) A transparent sheet or a topcoat of transparent sheets comprising the ultraphobic surface claimed in Claim 1.

Claim 16. (Withdrawn) Process for the preparation of a surface having ultraphobic properties according to claim 1 based on an $AlMg_3$ alloy, comprising cleaning, pickling,

anodically oxidating, passivating in boiling water, and optionally coating with a noble metal as an adhesion promoter, and coating with a hydrophobic material.

Claim 17. (Withdrawn) Process for the preparation of a surface having ultraphobic properties comprising molding, wherein a mould, which has the negative of a surface topography suitable for an ultraphobic surface, is moulded with a mixture of a plastic and a hydrophobic additive, which separates out upon curing as a thin film between the surface of the mould and the plastic moulding.

Claim 18. (Withdrawn) Process for the preparation of a surface having ultraphobic properties comprising moulding a surface of a positive mould, which has a surface structure suitable for an ultraphobic surface, with a plastic, and the surface of the resulting moulding having the negative impression of the surface of the positive mould is optionally provided with an adhesion promoter layer and then with a hydrophobic coating.

Claim 19. (Withdrawn) Process according to Claim 18, wherein the plastic is a hydrophobic polymer, and the additional coating with hydrophobic or oleophobic material is optionally omitted.

Claim 20. (Withdrawn) Process according to Claim 17, wherein the mould is the negative of the surface structure of a pickled, anodized surface consisting essentially of aluminium or an aluminium alloy and treated with hot water at from 50 to 100°C.

Claim 21. (Withdrawn) Process according to Claim 17, wherein the mould is the negative of the surface structure of a microstructured, anodized, calcined surface consisting essentially of aluminum or an aluminium alloy.

Claim 22. (Withdrawn) Process according to Claim 17, wherein the plastic used for the moulding is a thermosetting polymer or a thermoplastic polymer.

Claim 23. (Withdrawn) Process according to Claim 22, wherein the thermosetting polymer is selected from the group consisting of diallyl phthalate resin, epoxy resin, urea-

formaldehyde resin, melamine-formaldehyde resin, melamine-phenol-formaldehyde resin, phenol-formaldehyde resin, polyimide, silicone rubber and unsaturated polyester resin.

Claim 24. (Withdrawn) Process according to Claim 22, wherein the thermoplastic polymer is selected from the group consisting of thermoplastic polyolefin, polypropylene, polyethylene, polycarbonate, polyester carbonate, polyester, PBT, PET, polystyrene, styrene copolymer, SAN resin, rubber-containing styrene graft copolymer, ABS polymer, polyamide, polyurethane, polyphenylene sulphide, polyvinyl chloride and mixtures of said polymers.

Claim 25. (Withdrawn) Process according to Claim 17, wherein the surface of the moulding with the impression has a coating with a hydrophobic phobicization auxiliary, or phobicization auxiliary which hydrophobicizes the surface, used as additive to polymers compatible therewith.

Claim 26. (Withdrawn) A method of testing a surface for ultraphobic properties, comprising coating the surface with a noble metal or GaAs as adhesion promoter, further coating with a phobicization auxiliary, then analyzing the surface topography and, from the measured data, the spatial frequencies f and their structure amplitudes a(f), and the integral of the function S

$$S(\log F)=a(f){\cdot}f \tag{1}$$

calculated between the integration limits $\log(f_1/\mu m^{-1})$=-3 and $\log(f_2\mu m^{-1})$=3 is formed.

Claim 27. (Previously Presented) The surface according to Claim 1, wherein said surface comprises a thermoplastic polymer and is selected from the group consisting of polyolefins, polypropylene, polyethylene, polycarbonates, polyester carbonates, polyesters, PBT, PET, polystyrene, styrene copolymers, SAN resin, rubber-containing styrene graft copolymers, ABS polymer, polyamides, polyurethanes, polyphenylene sulphide, polyvinyl chloride and mixtures thereof.

Claim 28. (Previously Presented) The surface according to claim 1, wherein said surface comprises a coating of a hydrophobic phobicization auxiliary which comprises a group which is an anionic, cationic, amphoteric or nonionic, interface active group.

Claim 29. (Withdrawn) The self-cleaning coating or panelling of building structures, roofs, windows, ceramic construction material claimed in Claim 13 for sanitary installations and household applicances.

Claim 30. (Withdrawn) The transparent sheet of Claim 15 used as a sheet or top-coating in glass or plastic.

Claim 31. (Withdrawn) The transparent sheet of Claim 15 used as a sheet or top-coating for solar cells, vehicles, or greenhouses.

Claim 32. (Withdrawn) The process of Claim 16, wherein the noble metal coating is gold with a layer thickness of from 10 to 100 nm.

Claim 33. (Withdrawn) The process of Claim 32, wherein the coating is prepared by atomization.

Claim 34. (Withdrawn) The process of Claim 16, wherein the hydrophobic material is a phobicization auxiliary selected form the group consisting of anionic, cationic, amphoteric, and nonionic interface active compounds.

Claim 35. (Withdrawn) The process claimed in Claim 17, wherein the hydrophobic additive is oleophobic.

Claim 36. (Withdrawn) The process as claimed in Claim 18, wherein the plastic is a thermosetting or thermoplastic polymer.

Claim 37. (Withdrawn) The process as claimed in Claim 18, wherein the hydrophobic coating is oleophobic.

Claim 38. (Withdrawn) The process as claimed in Claim 19, wherein the hydrophobic polymer is poly(methyl)methacrylate-co-perfluorooctadecyl methacrylate.

Claim 39. (Withdrawn) Process according to Claim 18, wherein the mould is the positive of the surface structure of a pickled, anodized surface consisting essentially of aluminium or an aluminium alloy and treated with hot water at from 50 to 100°C.

Claim 40. (Withdrawn) Process according to Claim 18, wherein the mould is the positive of the surface structure of a microstructured, anodize, calcined surface consisting essentially of aluminum or an aluminium alloy.

Claim 41. (Withdrawn) Process according to Claim 18, wherein the plastic used for the moulding is a thermosetting polymer or a thermoplastic polymer.

Claim 42. (Withdrawn) Process according to Claim 41, wherein the thermosetting polymer is selected from the group consisting of diallyl phthalate resin, epoxy resin, urea-formaldehyde resin, melamine-formaldehyde resin, melamine-phenol-formaldehyde resin, phenol-formaldehyde resin, polyimide, silicone rubber and unsaturated polyester resin.

Claim 43. (Withdrawn) Process according to Claim 41, wherein the thermoplastic polymer is selected from the group consisting of thermoplastic polyolefin, polypropylene, polyethylene, polycarbonate, polyester carbonate, polyester, PBT, PET, polystyrene, styrene copolymer, SAN resin, rubber-containing styrene graft copolymer, ABS polymer, polyamide, polyurethane, polyphenylene sulphide, polyvinyl chloride and mixtures of said polymers.

Claim 44. (Withdrawn) Process according to Claim 18, wherein the surface of the moulding with the impression has a coating with a hydrophobic phobicization auxiliary, or phobicization auxiliary which hydrophobicizes the surface, used as additive to polymers compatible therewith.

Claim 45. (Withdrawn) The process according to Claim 17, wherein the hydrophobic auxiliary is an anionic, cationic, amphoteric, or nonionic interface active compound.

Claim 46. (Withdrawn) The process according to Claim 18, wherein the hydrophobic auxiliary is an anionic, cationic, amphoteric, or nonionic interface active compound.

Claim 47. (Withdrawn) The method claimed in Claim 26, wherein said surface is coated by vapor deposition.

Claim 48. (Withdrawn) The method claimed in Claim 26, wherein the adhesion promoter is gold.

Claim 49. (Withdrawn) The method claimed in Claim 48, wherein the gold layer has a thickness of 10 to 100 nm.

Claim 50. (Withdrawn) The method claimed in claim 26 wherein the phobicization auxiliary is decanethiol.

Claim 51. (Withdrawn) The method claimed in Claim 26, wherein the surface topography is analyzed with a combination of scanning tunneling microscopy, scanning atomic force microscopy, and/or white light interferometry.

Claim 52. (Previously Presented) A surface having ultraphobic properties, comprising a surface topography in which the value of the integral of a function S

$$S(\log f) = a(f) \cdot f \qquad (1),$$

which gives a relationship between the spatial frequencies F of the individual Fourier components and their amplitudes a(f), is at least 0.5 between the integration limits $\log(f_1/\mu m^{-1})=-3$ and $\log(f_2/\mu m^{-1})=3$, wherein said surface comprises a hydrophobic material, or is coated with a hydrophobic material.

Claim 53. (Previously Presented) A surface having ultraphobic properties, comprising a surface topography in which the value of the integral of a function S

$$S(\log f) = a(f) \cdot f \qquad (1),$$

which gives a relationship between the spatial frequencies F of the individual Fourier components and their amplitudes a(f), is at least 0.5 between the integration limits

$\log(f_1/\mu m^{-1}) = -3$ and $\log(f_2/\mu m^{-1}) = 3$, wherein said surface comprises an oleophobic material, or is coated with an oleophobic material.

Claim 54. (Previously Presented) The surface according to claim 1, wherein said surface comprises a metal and is $AlMg_3$.

Roughness analysis of optical films and substrates by atomic force microscopy

C. Ruppe [1], A. Duparré *

Fraunhofer Institute for Applied Optics and Precision Engineering, IOF Schillerstrasse 1, D-07745, Jena, Germany

( )

(/

Fraunhofer Institut
Angewandte Optik
und Feinmechanik

Angela Duparré   Schillerstraße 1
Dr. rer. nat. Dipl.-Phys.   D-07745 Jena   216
    Systeme   Telefon +49 (0) 36 41 / 8 07-303
Abteilung Optische Schichten   Telefax +49 (0) 36 41 / 8 07-601
Gruppenleiterin Schicht- und   email: duparre@iof.fhg.de   602
Oberflächen-Charakterisierung   http://www.iof.fhg.de

ELSEVIER

Roughness analysis of optical films and substrates by atomic force microscopy

C. Ruppe [1], A. Duparré *

Fraunhofer Institute for Applied Optics and Precision Engineering, IOF Schillerstrasse 1, D-07745, Jena, Germany

Abstract

From atomic force microscopy (AFM) topographic data, the power spectral densities (PSDs) of substrate and film surfaces were calculated over extended bandwidths. The results were successfully compared with PSDs obtained from angle-resolved scattering (ARS) measurements, while considering the overlapping spectral frequency range of both methods. The PSD curves obtained by AFM also proved to be a suitable tool for investigating the influence of the substrate on the surface topography of thin film coatings. A correlation factor quantifying the relation between the substrate and film PSD is suggested as a measure of substrate replication effects after thin film deposition.

Keywords: Atomic force microscopy; Light scattering; Optical thin films; Surface roughness

1. Introduction

The quality of optical thin film components is substantially influenced by their microtopography. In particular, optical losses due to light scattering are largely dominated by surface and interface roughnesses. Hence a detailed knowledge of the roughness characteristics of both substrates and thin films will aid in the optimization of the production parameters of the optical coating.

Of the variety of instruments and methods capable of measuring the surface roughness of thin film components, we believe that light scattering and atomic force microscopy (AFM) are excellent tools for meeting the specific requirements of such samples. For about two decades, numerous investigations have been dedicated, both experimentally and theoretically, to the problem of roughness and light scattering (see, for example, Refs. [1–10]), but AFM is still in the early stages of becoming an accepted method of roughness investigation in the optical area [11–15]. Surface microtopography studies have so far focused on materials for several non-optical applications, such as silicon, metals and tribological films [16–21].

In most cases where optical surfaces are to be evaluated, the parameter commonly used for describing the roughness characteristics of a bare surface or coating is the root-mean-square (rms) roughness. It very rapidly conveys to the user an impression of the quality of the surface under study and, as long as the bandwidth-limited character of this quantity is taken into account appropriately, it represents a suitable tool for roughness description. However, when specific roughness properties have to be investigated in detail, spectral roughness analysis should be performed. Determining the power spectral density (PSD) provides valuable information not only on the height deviation of the roughness profile, but also on its lateral distribution [1], and hence it gives a more general description than the rms roughness alone. In recent papers [11,15], this approach has been successfully applied to AFM data obtained on optical surfaces, while extending the PSD consideration over a large bandwidth.

In this paper, after providing a short explanation of the theoretical tools and experimental background, results of AFM topographic measurements on BK7 glasses and subsequent PSD calculations over a wide spatial frequency spectrum are presented. In the frequency range in which the bandwidth of AFM overlaps that of angle-resolved scattering (ARS), the spectral roughness curves of BK7 and multilayer coatings are compared. Eventually, using PSD curves obtained from AFM measurements, we study how the roughness characteristics of substrates are modified after the evaporation of a two-layer film or, in other words, how much correlation remains between the coated and uncoated surfaces. Such questions have been comprehensively discussed earlier within the framework of light scattering investigations [2,3,9,10].

---

* Corresponding author.

[1] During the preparation of this work, C. Ruppe was a student at IOF, Jena. He is now with OCLI, Goslar, Germany.
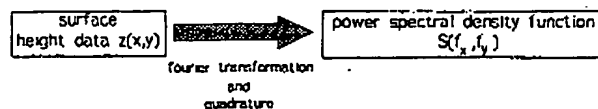
9

9

Fig. 1. Schematic diagram of the PSD calculation procedure.

2. Determination of the PSD functions

As there are a large number of papers and books dealing generally and comprehensively with the description of surface statistics [1,22,23], we only briefly outline the specific methods used in our PSD determination program. On the basis of the surface statistical treatment in Ref. [22], a home-made computer program for quantitative analysis of the microtopography as recorded by AFM was developed as described below (see also Fig. 1).

A two-dimensional fast Fourier transform algorithm was applied to the AFM image data, followed by the calculation of the square and normalization to the scanned area

$$S_2(f_x, f_y) = \frac{1}{L^2} \left[\sum_{m=1}^{N} \sum_{n=1}^{N} z_{mn} e^{-2\pi i \Delta L (f_x m + f_y n)} (\Delta L)^2 \right]^2 \quad (1)$$

where S_2 denotes the two-dimensional PSD, L^2 is the scanned surface area, N is the number of data points per line and row, z_{mn} is the profile height at position (m, n), $f_{x,y}$ is the spatial frequency in the x and y directions and $\Delta L = N/L$ is the sampling distance.

This was followed by transition to polar coordinates in frequency space and angular averaging ({varphi})

$$S_2(f) = \frac{1}{2\pi} \int_0^{2\pi} S_2(f, \varphi) \, d\varphi \quad (2)$$

As the PSD function depends on only one parameter, it is plotted in all figures as a "slice" of the two-dimensional representation. However, it remains a two-dimensional function with the unit (length⁴).

3. Experimental implementation

To investigate the substrates and film surfaces, a DIMENSION 3000 atomic force microscope was operated in Contact mode. This specific NanoScope III instrument (Digital Instruments) is capable of performing measurements in various modes, such as Contact, Tapping™ and Lateral Force, even on large samples. This is especially important as the majority of our investigations deal with optical components, such as laser mirrors and their substrates, Anti Reflective (AR) coatings and lenses, the diameters of which range from a few millimetres to hundreds of millimetres.

The reason for using, for these particular experiments, the Contact mode rather than Tapping™ is simply that, as far as glass substrates were concerned, we had already gained quite a lot of experience with this mode when starting to operate the new Tapping™ mode. Hence, for consistency, we

decided to finish the series of PSD experiments using the Contact mode, even though the Tapping™ mode has proved to be a very suitable tool for examining our optical film components.

Si tips with tip radii of approximately 10 nm were used for all measurements. AFM topographic images were recorded over scan areas from 1 μm × 1 μm to 80 μm × 80 μm, each with a resolution of 512 × 512 data points. With $f_{max} = 1/2\Delta L = N/2L_{min}$, the theoretical value of the highest spatial frequency contributing to the roughness calculation is 256 μm⁻¹, which is tantamount to a lowest spatial wavelength of $d_{min} \approx 4$ nm. The long range limit of the spatial wavelength d_{max} is attributed to the largest scan length L_{max}, i.e. 80 μm (corresponding to a low spatial frequency limit of $1/L_{max} = 0.0125$ μm⁻¹). Instrumental artefacts such as those caused by the curvature of the piezo movement, as well as effects of thermal drifts and lateral forces, are usually superimposed on the image. In order to eliminate these artificial roughness contributions, a third-order polynomial was fitted to each scan line and afterwards subtracted (procedure called "flatten").

For comparison, a few samples were also investigated by angle-resolved light scattering, and PSDs were calculated from the scattering curves in the following way. In the case of normal incidence and a single boundary (optical surface/air), the two-dimensional PSD is given by the relation [22]

$$ARS = \frac{dP/d\Omega}{P_i} = \frac{16\pi^2 Q}{\lambda^4} S_2(f) \quad (3)$$

where $dP/d\Omega$ represents the scattered power per solid angle element, $d\Omega = \sin \theta \, d\theta d\varphi$, P_i is the incident power, λ is the wavelength, θ is the polar scattering angle, {varphi} is the azimuthal angle and Q is the optical factor.

Backscattering measurements were carried out at 623.8 nm using the ARS equipment described in detail in Ref. [24]. The measurements were performed at normal incidence with a low scattering angle limit of 2°. Then, from $\sin \theta = f\lambda$, $\theta_{min} = 2°$ and $\theta_{max} = 90°$, the lower and upper spatial frequency limits were determined as 0.06 μm⁻¹ and 1.6 μm⁻¹ respectively.

4. Sample preparation

In our experiments, conventionally polished BK7, quartz glass and MgF₂ substrates (diameter, 2.5 cm; thickness, 5 mm) were used. MgF₂ single layers and MgF₂/LaF₃ multilayer systems were evaporated at a substrate temperature of 400 °C from resistance heated boats. In one case, a fluoride multilayer was overcoated with a thin aluminium layer (thickness, 75 nm) using magnetron sputtering. This opaque cover layer was necessary to obtain pure surface roughness information from light scattering measurements. In previous investigations, such Al films proved to be very suitable for replicating the underlying microstructure of fluoride films correctly, i.e. without adding any remarkable roughness

10

10

[25]. The thicknesses and multilayer configurations of the fluoride films used in the experiments are given, together with a discussion of the results, in Section 5.

5. Results and discussion

Fig. 2 shows the PSD curves obtained from AFM images of a BK7 surface on varying the scan size from 1 μm$\times$1 μm to 80 μm$\times$80 μm. As an example, the top-view image of the 40 μm$\times$40 μm scan is displayed in Fig. 3. The PSD curves

calculated for each AFM image overlap at the intersections of the particular frequency intervals. Due to the "flatten" procedure applied to the AFM data, the amplitudes at the low spatial frequency limits of each particular scan decrease. Unfortunately, there is no analytical expression to determine how this affects the PSD value at low frequencies. From experience, it is reasonable to cut the curves for frequencies lower than 1.5% of the highest frequency of each scan.

Fig. 4 shows the results of a comparison between PSD functions as determined by AFM and ARS within the same spatial frequency range for an uncoated BK7 substrate and a
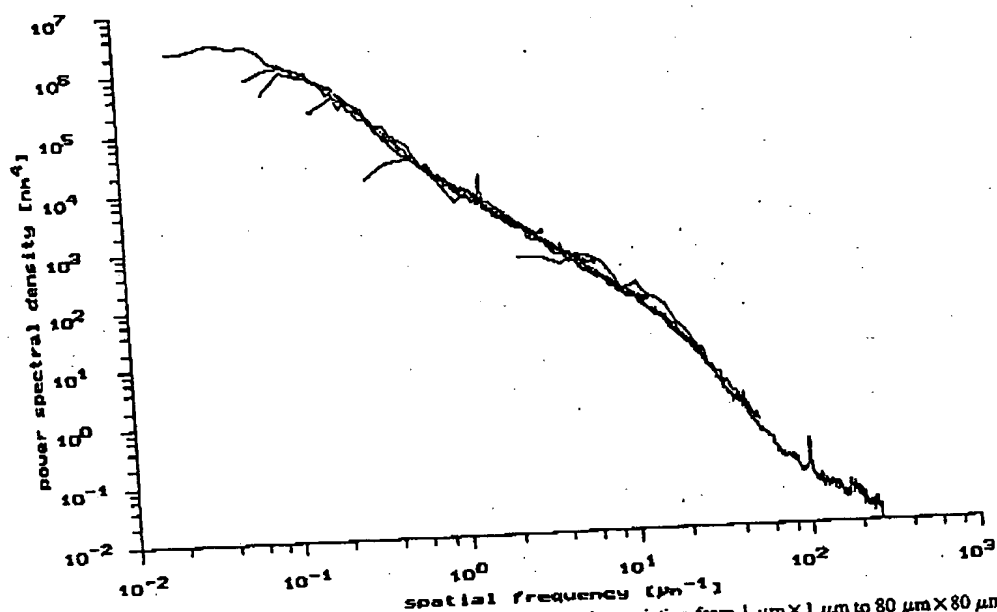

Fig. 2. PSD curves of a BK7 surface obtained from AFM data. Scan size variation from 1 μm$\times$1 μm to 80 μm$\times$80 μm.
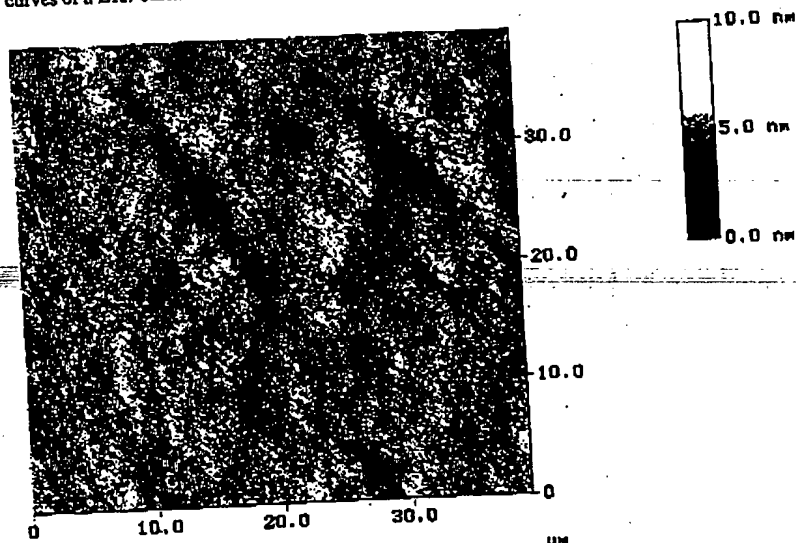

Fig. 3. AFM top-view image of the surface corresponding to Fig. 2 (40 μm$\times$40 μm scan).
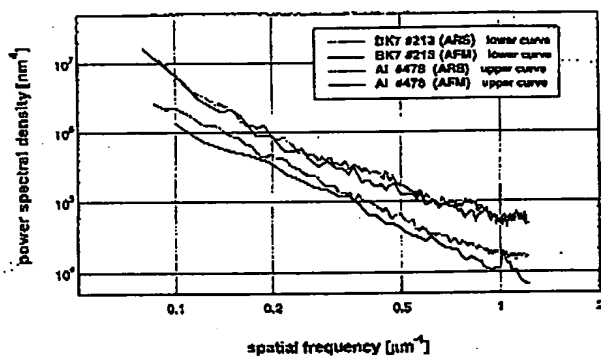
11

11

Fig. 4. Comparison of PSD curves obtained from AFM and ARS measurements on a BK7 surface (213) and aluminized multilayer coating (478).

dielectric coating with an Al cover layer. The dielectric coating consisted of a five-layer system of alternating MgF$_2$/LaF$_3$ films with half-wave optical thicknesses at a design wavelength $\lambda = 248$ nm. The results of AFM and ARS are in good agreement. In fact, the PSD curves of the aluminized layer system coincide. For the BK7 surfaces, the PSD values calculated from ARS measurements slightly exceed those determined from AFM, which can be explained as a result of the well-known problem of scattering contributions from the rear of transparent samples.

Remarkable differences are obtained regarding the shapes of the PSD functions of pure substrates and thin films when considering an extended spatial frequency range (see Fig. 5). The substrate curves reveal a linear form in the log–log plot, which is a typical but not strict characteristic of glass surfaces [18,26,27]. In contrast, the thin film roughness gives rise to a "knee" in the higher frequency interval [27]. Both films were single layers of MgF$_2$ with geometrical thicknesses of 225 nm and 459 nm respectively. Owing to the larger film thickness of sample 208, the development of the columnar structure results in a higher roughness level. The PSD of sample 2/590 displays a substrate-like behaviour at frequencies below 1 μm^{-1}, whereas for sample 208 the transition frequency to the substrate type occurs around 0.2 μm^{-1}. This

shift to shorter spatial frequencies is attributed to the larger columnar structures of the thicker film, which not only cause a higher vertical roughness, but also enhanced lateral dimensions [2].

As a first approach to the quantitative measurement of the influence of the substrate roughness on the topography of the coating, i.e. quantifying the degree of roughness replication, we simply used a "correlation factor" that is common in general statistical descriptions

$$\kappa = \frac{\sum_{i=1}^{N} (S_s(f_i) - \bar{S}_s)(S_C(f_i) - \bar{S}_C)}{\sqrt{\sum_{i=1}^{N} (S_s(f_i) - \bar{S}_s)^2 \sum_{i=1}^{N} (S_C(f_i) - \bar{S}_C)^2}} \qquad (4)$$

where κ is the correlation factor, S_s and S_C denote the PSDs of the substrate and coating respectively and $\bar{S}_s$ and $\bar{S}_C$ are the corresponding averaged PSDs.

It should be emphasized that κ must not be confused with the degree of cross-correlation that can be determined from light scattering investigations [3]. Cross-correlation as calculated from scattering actually relates the surface roughness profile of a dielectric thin film coating (film/air interface) to the substrate profile (substrate/film interface). This is accomplished by utilizing interference effects of scattering between the two interface profiles, so that phase information and hence the true relation of the two profiles to each other are maintained. In contrast, κ provides a pure statistical description of the "similarity" between the two surfaces without including any phase information.

The correlation factor was calculated from AFM PSD data of an MgF$_2$/LaF$_3$ coating ($\lambda/4$ layers, $\lambda = 248$ nm) on quartz and MgF$_2$ substrates (see Fig. 6). The low and high spatial frequency limits were set at 0.15 μm^{-1} and 12.8 μm^{-1}. $\kappa = 0.9$ and $\kappa = 0.7$ were obtained for the coating on the MgF$_2$ and quartz substrates respectively. The correlation is very high in the case of the rough magnesium fluoride substrate, with the coating almost entirely replicating the surface morphology in the lower frequency range and a similarity between the film and substrate morphology in the higher frequency range. This situation can be seen qualitatively from the AFM top-view image in Fig. 7 where, in addition to the typical surface features of the columnar film structure, surface defects of the substrate, such as scratches, can be easily recognized. With the much smoother quartz substrate, correlation is less pronounced (see also the missing surface defects in Fig. 7, left), but still present through the contribution at small frequencies.

It should be emphasized that the correlation factor is subject to bandwidth limitation (as are all roughness values) and provides meaningful values only in the context of the spatial frequency limits given.

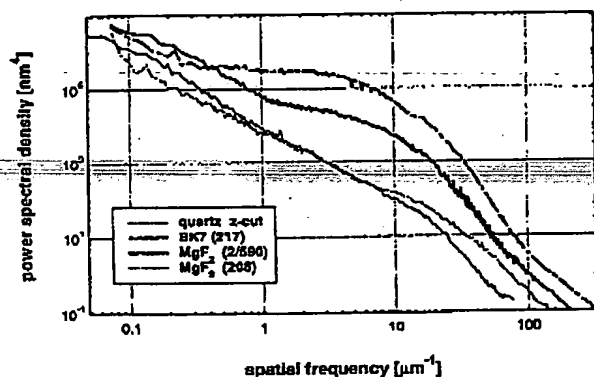

Fig. 5. PSD curves calculated from AFM measurements on substrates and MgF$_2$ single layers. Geometrical film thicknesses: 225 nm (2/590); 490 nm (208).

6. Conclusions

The PSD functions of different substrates and optical coatings were evaluated from AFM data. To extend the spatial

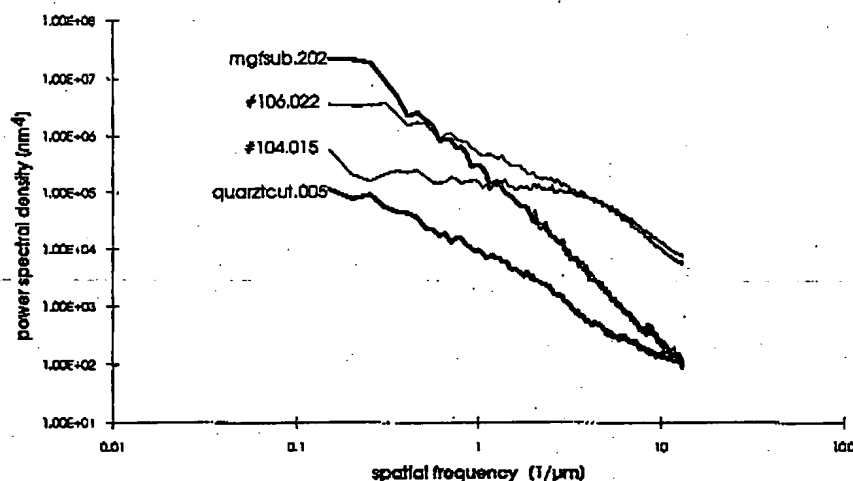Fig. 6. PSD curves calculated from the AFM data of an MgF$_2$/LaF$_3$ double layer on MgF$_2$ (106.022) and quartz (104.015), together with the curves for the pure substrates (mgfsub, quartzcut).

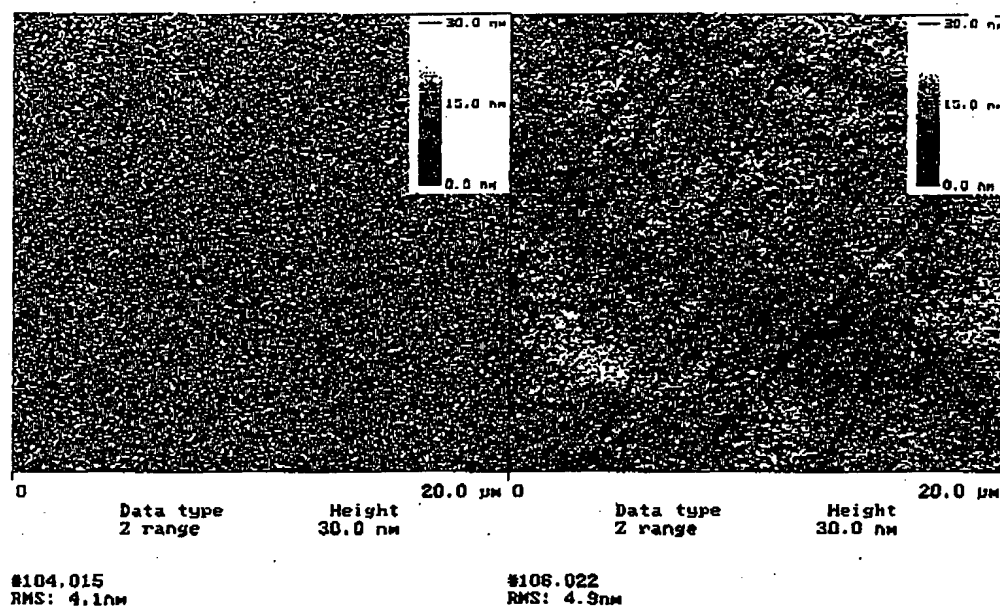#104.015
RMS: 4.1nm

#106.022
RMS: 4.9nm

Fig. 7. AFM top-view images of samples 106 (right) and 104 (left).

frequency limits of AFM images, several images with different scan sizes were performed. As an example, it was demonstrated for BK7 surfaces that, through appropriate scan size variation and overlapping of the particular PSDs, the overall frequency range can be considerably extended. Comparison with PSD functions calculated from ARS measurements showed good agreement between the results obtained from the non-optical and optical method. A parameter has been suggested that describes the correlation (similarity) between the PSDs of a coating and its substrate. It provides a simple quantitative measure of the influence of the substrate roughness on the coating.

Acknowledgements

References

[1] J.M. Bennett and L. Mattsson, *Introduction to Surface Roughness and Scattering*, Optical Society of America, Washington DC, 1989.

13

[2] A. Duparré, Light scattering of thin dielectric films, in R.E. Hummel and K.H. Günther (eds.), Thin Films for Optical Coatings, CRC Press, Boca Raton, FL, London, Tokyo, 1995.

[3] C. Amra, Light scattering from multilayer optics. I. Tools of investigation. II. Application to experiment, J. Opt. Soc. Am. A, 11 (1994) 197–226.

[4] A. Duparré and S. Kassam, Relation between light scattering and the microstructure of optical thin films, Appl. Opt., 32 (1993) 5475.

[5] P. Bousquet, F. Flory and P. Roche, Scattering from multilayer thin films: theory and experiment, J. Opt. Soc. Am., 71 (1981) 1115–1123.

[6] C.K. Carniglia, Scalar scattering theory for multilayer optical coatings, Opt. Eng., 18 (1979) 104–115.

[7] J.M. Elson, J.P. Rahn and J.M. Bennett, Light scattering from multilayer optics: comparison of theory and experiment, Appl. Opt., 19 (1980) 669–679.

[8] A. Duparré, S. Gliech, K. Hehl, S. Pichlmaier and U. Schuhmann, Interface and volume inhomogeneities in optical thin films investigated by light scattering methods, Int. Symp. on Optical Interference Coatings, 6–10 June 1994, Grenoble, Proc. SPIE, 2253 (1994) 1060–1069.

[9] C. Amra, P. Roche and E. Pelletier, Interface roughness cross-correlation laws deduced from scattering diagram measurements on optical multilayers: effect of the material grain size, J. Opt. Soc. Am. B, 4 (1987) 1087–1093.

[10] A. Duparré and H.G. Walther, Surface smoothing and roughening by thin film deposition, Appl. Opt., 27 (1988) 1393–1395.

[11] Ph. Dumas, B. Bouffakhreddine, C. Amra, O. Vatel, E. Andre, R. Galindo and F. Salvan, Quantitative microroughness analysis down to the nanometer scale, Europhys. Lett., 22 (1993) 717–722.

[12] J.M. Bennett, J. Jahannir, J.C. Podlesny, T.L. Balter and D.T. Hobbs, Scanning force microscopy as a tool for studying optical surfaces, Appl. Opt., 43 (1995) 213–230.

[13] A. Duparré, N. Kaiser, H. Truckenbrodt, M. Berger and A. Köhler, Microtopography investigations of optical surfaces and thin films by light scattering, optical profilometry, and atomic force microscopy, Int. Symp. on Optics, Imaging and Instrumentation, 11–16 July 1993, San Diego, CA, Proc. SPIE, 1995 (1993) 181–192.

[14] A. Duparré, N. Kaiser and S. Jakobs, Morphology investigations by atomic force microscopy of thin films and substrates for excimer laser mirrors, Annual Symp. on Optical Materials for High Power Lasers, 27–29 October 1993, Boulder, CO, Proc. SPIE, 2114 (1993) 394.

[15] C. Amra, C. Deumie, D. Torricini, P. Roche, R. Galindo, P. Dumas and F. Salvan, Overlapping of roughness spectra measured in macroscopic (optical) and microscopic (AFM) bandwidths, Int. Symp. on Optical Interference Coatings, 6–10 June 1994, Grenoble, Proc. SPIE, 2253 (1994) 614–630.

[16] T. Abe, E.F. Steigmeier, W. Hagleitner and A.J. Pidduck, Microroughness measurement on polished silicon wafers, Jpn. J. Appl. Phys., 31 (1992) 721–728.

[17] Y.E. Strausser, B. Doris, A.C. Diebold and H.R. Huff, Measurement of silicon surface microroughness by AFM, Proc. 185th Meeting of the Electrochemical Society, May 22–27 1994, San Francisco, Electrochemical Society (1994).

[18] O. Vatel, P. Dumas, F. Chollet, F. Salavan and E. André, Roughness assessment of polysilicon using power spectral density, Jpn. J. Appl. Phys., 32 (1993) 5671–5674.

[19] Y. Carmi, A.J. Dahm, S.J. Eppell, W. Jannings, R.E. Marchant and G.M. Michal, Atomic force microscopy and Auger electron microscopy studies of thin ultrasmooth Au–Cr films on mica, J. Vac. Sci. Technol. B, 10 (1992) 2302–2306.

[20] K.L. Vestra and D.J. Thomson, The microstructure of thin films observed using atomic force microscopy, Thin Solid Films, 257 (1995) 15–21.

[21] K.A. Pischow, A.S. Korhonen and E.O. Ristolainen, SFM and SIMS study of tribofilms growing on TiN coatings during an elevated temperature test, in M.S.J. Hashmi (ed.), Proc. AMPT-93, 1993, pp. 1887–1895.

[22] J.C. Stover, Optical scattering, measurement and analysis, in R.E. Fischer and W.J. Smith (eds.), Optical and Electro-optical Engineering Series, McGraw-Hill, New York, Hamburg, Paris, London, Tokyo, 1990.

[23] D.J. Whitehouse, Handbook of Surface Metrology, Institute of Physics Publishing, Bristol, Philadelphia, 1994.

[24] H. Truckenbrodt, A. Duparré and U. Schuhmann, Roughness and defect characterization of optical surfaces by light scattering measurements, Proc. SPIE, 1781 (1992) 139–151.

[25] A. Duparré and S. Kassam, Relation between light scattering and the microstructure of optical thin films, Appl. Opt., 32 (1993) 5475–5480.

[26] E.L. Church, Fractal surface finish, Appl. Opt., 27 (1988) 1518–1526.

[27] A. Duparré, Combination of surface characterization techniques for proper investigation of optical thin film morphology, Int. Conf. on Optical Interference Coatings, 5–9 June 1995, Tucson, AZ, 1995 Technical Digest Series, 17, Optical Society of America (1995) 176.

14

S.N. Magonov und M.-H. Whangbo, Surface Analysis with STM and AFM

VCH, Weinheim 1996, XII + 323 S.

ISBN 3-537-29313-2

Seite 47-63

Full length article

Analysis of white light interferograms using wavelet methods

Rolf-Jürgen Recknagel *, Gunther Notni

Fraunhofer-Institution for Applied Optics and Precision Engineering Jena, Schillerstraße 1, D-07745 Jena, Germany

Abstract

Several methods for the analysis of white light interferograms are presented and their performance is compared to a new method employing the wavelet transform in connection with sub-Nyquist sampling. As the result of computer simulations and experiments the wavelet method proves to be best suited to the problem. © 1998 Elsevier Science B.V.

Keywords: White light interferometry: Wavelet transform: Surface profile measurement

1. Introduction

Quality control in microsystem technology, microoptics and machined surfaces demand to an increasing extent the measurement and characterisation of the finishing of both rough and highly reflecting surfaces. White light interferometry is an elegant method for measuring surface profiles and thickness of transparent materials [1–10]. It is also reported that white light interferometry has been used for material identification. In contrast to coherent interferometric techniques, white light interferograms (correlation function, correlogram) have a very small spatial extend and can thus be used to determine the position of the zero path difference without any phase ambiguity. Hence height measurement ranges of several hundred micrometers are possible. The path difference is changed by means of a piezo actuator in order to record the interferograms. The position of the highest contrast in the correlogram corresponds to the position of zero path difference and is given by the position of the envelope peak of the interferogram. The zero-order interference fringe can be used instead of the envelope peak if there is no dispersion and the object is homogeneous. Obviously, the accuracy of the change of path difference determines directly the achievable vertical accuracy of the interferometer.

In this work a method for the analysis of correlograms by means of a wavelet filter is presented and compared to conventional methods like the Fourier transform [1,2], the polynomial interpolation and the centre of gravity [3]. Whenever possible sub-Nyquist sampling is considered as well. Other methods not tested here are the low pass filtering employed by Caber [4], the Fourier method by Kino and Chim [5] which also filters the signal and a recently proposed method by Larkin [6] which uses nonlinear methods known from phase shift interferometry to detect the envelope. From the computational point of view the first two are prohibitive on normal PCs whereas the algorithm proposed by Larkin is very efficient but offers an intrinsic accuracy of only 1/20 of the sampling step size according to the author. This corresponds to an error of more than 10 nm in the sub-Nyquist case.

Computer simulations are used to determine the sensitivity to noise and the intrinsic systematic errors of the algorithms in the presence of sampling step size miscalibrations and the like. Additionally the achievable rms repeatability is determined experimentally and compared to the results of the computer simulations.

2. White light interferograms and analysis

A white light interferogram is basically given by

$$I(z) = I_0 + I_1 \cos(kz + \phi) \exp\left[-(z - z_m)^2/2w^2\right]. \quad (1)$$

* E-mail: recknag@iof.fhg.de

where z_m is the envelope peak position, w the width of the envelope, k the wavenumber, ϕ the phaseshift of the carrier frequency, I_0 the intensity of the offset and I_1 the modulation. The formula is derived assuming a Gaussian spectrum of the light source and absence of dispersion. A comparison of a measured correlogram to a synthetic one showed sufficient coincidence. Generally the envelope peak position is the position of highest visibility and thus corresponds to the surface height.

In the following all algorithms for the analysis of the correlograms considered in this paper are briefly described namely the Fourier method, the polynomial interpolation, the centre of gravity and the wavelet method. The wavelet algorithm is presented in more detail because it represents a new algorithm which is to be compared to the other methods. Additionally some explanations concerning sub-Nyquist sampling step sizes are given at the end of this section.

2.1. Fourier method [1,2]

The Fourier transform is the classical method and can be used for Nyquist and sub-Nyquist sampled correlograms. Here the phase information of the Fourier transformed correlogram is used to determine the position of the highest contrast which corresponds to the surface height. One obtains the following formula for the surface height z_m.

$$z_m = \frac{d\phi}{dk}\Big|_{k_m}$$
(2)

where ϕ is the phase of the transformed correlogram and k_0 the mean wavenumber of the correlogram. Using the stated formula the peak position of the envelope of the correlogram is determined. Alternatively the position of the central fringe can be calculated from the transform provided the mean wavenumber k_0 is known precisely.

2.2. Polynomial interpolation

Another method to determine the position of the central fringe in a subpixel resolution is by means of a polynomial interpolation. Although it only works for Nyquist sampled signals the calculation can be done during the measurement process because of the simplicity of the algorithm. The surface height z_m is then given by

$$z_m = i + \frac{I_{i-1} - I_{i+1}}{2I_{i-1} - 4I_i + 2I_{i+1}}.$$
(3)

where I_i is the intensity of the correlogram at the position i.

2.3. Centre of gravity [3]

The centre of gravity is a method to determine the envelope peak position of Nyquist and also sub-Nyquist sampled correlograms but then with a decreased accuracy. Its accuracy is still sufficient to be used as an estimate for the wavelet filter algorithm. The surface height z_m can be found by

$$z_m = \frac{\sum_{i=1}^{N} i|I_i|I}{\sum_{i=1}^{N} |I_i|}.$$
(4)

2.4. Wavelet method [7]

Now the continuous wavelet transform is used for the analysis of the correlograms. It is defined as follows [11,12]

$$W_1(a,b) = \sqrt{a}\int_{-\infty}^{\infty} h^*(az - b)I(z)dz.$$
(5)

where $I(z)$ is the analysed signal, h the mother wavelet, a the scale factor and b the shift parameter. The Morlet wavelet is chosen as the mother wavelet because it exhibits the strongest similarity to the correlogram to be analysed [8]

$$h(z) = \exp(ik_0 z)\exp(-z^2/2).$$
(6)

The parameters of the correlograms such as the mean wavenumber and the width of the envelope do not vary more than about 10% which is less than the frequency resolution of the wavelet with those parameters. Consequently it is sufficient to calculate the transform only with the wavelet which has about the same mean frequency (wavenumber) as the correlogram, i.e. for just one scale factor. This is basically a filtering with an adapted filter which retains the main features of the correlogram but reduces the noise and asymetries of the envelope possibly introduced by dispersion of second order. The transformed correlogram W_1 is then

$$W_1(z') = \int_{-\infty}^{\infty} \exp[-ik_0(z - z')]$$
$$\times \exp[-(z - z')^2/2w^2]I(z)dz.$$
(7)

In practice the correlograms are given in a discrete form and therefore a discrete form of the wavelet has to be used as well. Possible sub-Nyquist step sizes are stated below. The real part of W represents the filtered correlogram whereas the envelope is given by the absolute modulus of W. In order to determine the position of the maximum of $Re(W)$ or $|W|$ in subpixel resolution a polynomial interpolation can be performed as described above.

Figs. 1–4 show the effect of wavelet filtering. In Fig. 1 a synthetic correlogram is seen, in Fig. 2 the same correlo-

124   R.-J. Recknagel. G. Notni / Optics Communications 148 (1998) 122–128
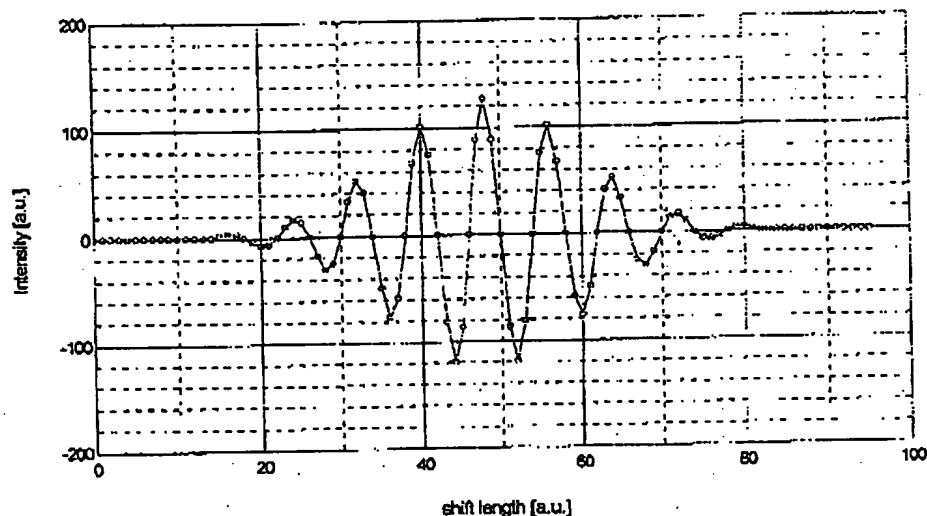
Fig. 1. Synthetic correlogram. Nyquist sampled with 0.25π.

gram with added intensity noise, in Fig. 3 the correlogram from Fig. 2 sub-Nyquist sampled and Fig. 4 shows the filtered correlogram. It is obvious that the original correlogram is reconstructed with nearly no noise, only the envelope is broadened by filtering.

In the following it is described how a sub-Nyquist sampling of a signal with a sinusoidal carrier can be performed [7]. The following sub-Nyquist (s-n) sampling step sizes ΔS can be used for a well defined sampling of a sinusoidal

$$\Delta S \approx \frac{2\pi n}{P}, \quad n|_{n \in N} \neq k|_{k \in N} \frac{P}{2}. \tag{8}$$

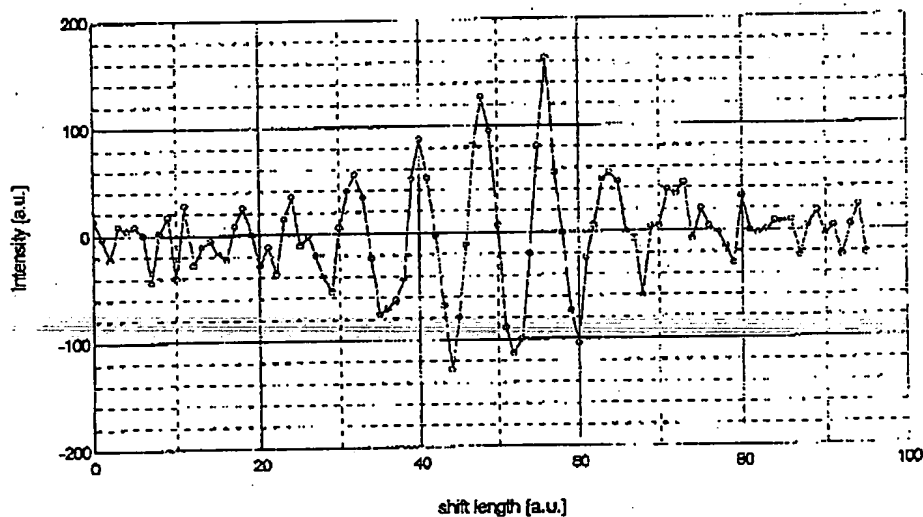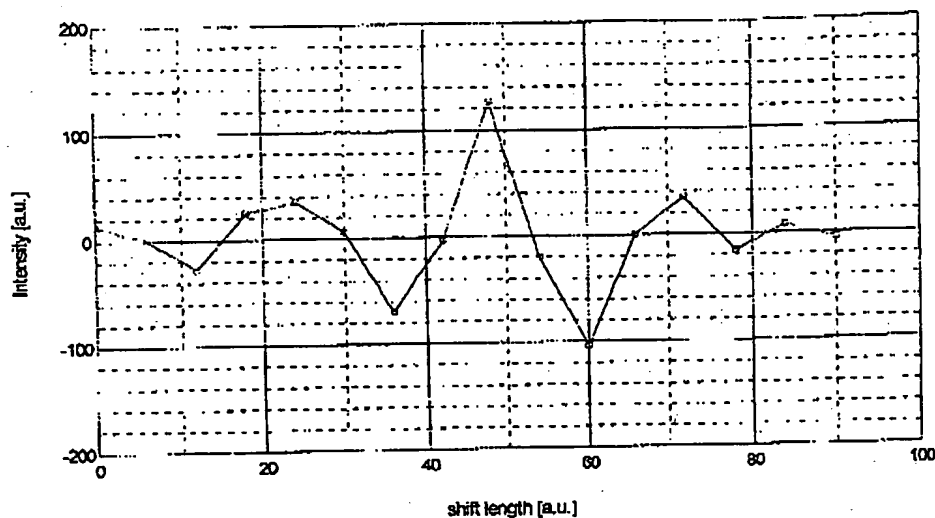where P is the number of samples per period and n is the

Fig. 2. Same correlogram as in Fig. 1 but with added noise (SNR = 10).

125

Fig. 3. Same correlogram as in Fig. 2 but sub-Nyquist sampled with 1.5π.

factor by which the frequency of the s-n sampled sinu-soidal is smaller than the one of the original signal.

The formula is a mathematical representation of the following idea: the number of samples per period of the s-n sampled signal multiplied by the s-n step size must be an integer multiple of the period of the original signal.

Additionally the s-n step size must not be an integer multiple of π which is taken into account by the given condition for n.

A signal consisting of a sinusoidal carrier with the (known) frequency f (wavelength $\bar{\lambda}$) and a slowly varying envelope can be s-n sampled if the step size is chosen
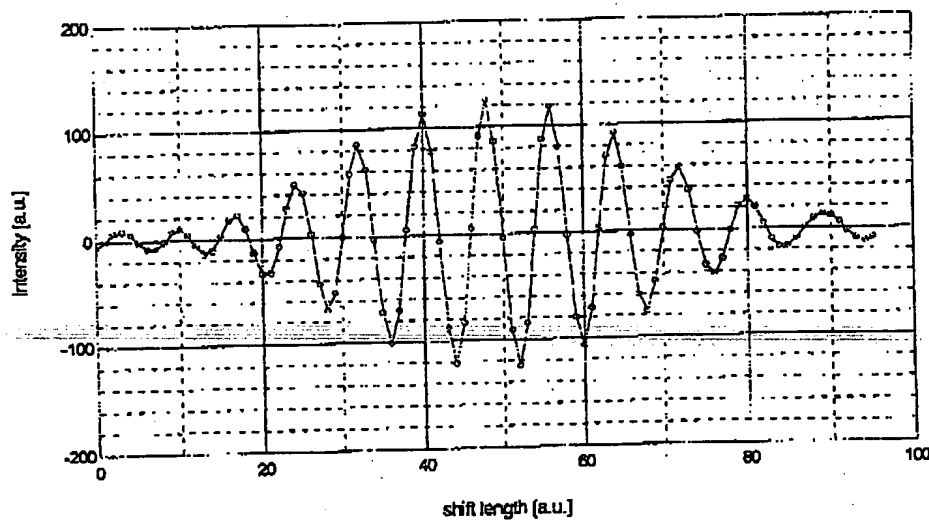
Fig. 4. Reconstructed correlogram Re(W) ((from correlogram in Fig. 3).

126.   R.-J. Recknagel, G. Notni / Optics Communications 148 (1998) 122-128

appropriately. The form of the envelope is preserved and the carrier frequency is reduced by a factor of $1/n$. Hence the spectrum of the signal is shifted from $\bar{f}$ to $\bar{f}/n$. The upper frequency limit of the shifted signal is thus

$$f_{max} = \frac{P}{2}\frac{\bar{f}}{n}. \tag{9}$$

After shifting back the signal the upper frequency limit of the sampling of the original signal is obtained,

$$f_{max} = \bar{f} + \frac{\bar{f}}{n}\left(\frac{P}{2} - 1\right). \tag{10}$$

This corresponds to a minimal wavelength of

$$\lambda_{min} = \bar{\lambda}\Big/\left(\frac{P/2 - 1}{n} + 1\right). \tag{11}$$

Assuming a Gaussian envelope (i.e. a symmetric Gaussian spectrum) it is best to choose the upper frequency limit of the sampling of the shifted signal (f_{max}) twice as big as its carrier frequency ($\bar{f}/n$) to achieve complete sampling. Hence one gets

$$f_{max} = \frac{P}{2}\frac{\bar{f}}{n} \overset{!}{=} 2\frac{\bar{f}}{n} \Rightarrow P = 4 \tag{12}$$

and thus possible sampling step sizes and corresponding

minimal wavelength of the used light source are given by

$$\Delta S = n\frac{\pi}{2}, n\text{ odd}; \quad \lambda_{min} = \frac{\bar{\lambda}}{1/n + 1}. \tag{13}$$

The following minimal wavelength/sampling step size pairs correspond to a mean wavelength of $\bar{\lambda} = 570$ nm of the used halogen lamp

$$\Delta S = 1.5\pi, \lambda_{min} = 428\,\text{nm}; \quad \Delta S = 2.5\pi, \lambda_{min}$$
$$= 475\,\text{nm}; \quad \Delta S = 3.5\pi, \lambda_{min} = 499\,\text{nm}. \tag{14}$$

By looking at the spectrum of a measured correlogram for a halogen lamp one sees that only a sampling step size of 1.5π ensures a complete sampling of the signal with respect to the frequency.

3. Simulations

First of all the algorithms are compared with respect to the maximum error they produce under otherwise perfect conditions. These conditions include variations of the sampling step size and influences of the limited width of the recording window. The algorithms are tested with synthetic correlograms as given below but without noise. As a

Table 1
Random errors of the tested algorithms in nm

Algorithm		Intensity noise SNR			Sampling noise [nm]		
		256	50	5	2	10	50
FFT central fringe 0.25π	rms	0.09	0.55	50	0.25	1.4	7.3
	pv	0.29	1.6	290	0.7	4.4	22
FFT envelope 0.25π	rms	1.4	6.2	64	1.2	6.5	45
	pv	3.3	17	164	4.1	16	150
FFT envelope 1.5π	rms	4.0	20	285	0.75	6.3	120
	pv	13	52	2300	2.4	28	730
Polynom 0.25π	rms	0.24	1.1	193	1.0	4.8	170
	pv	0.8	2.7	562	3.0	14	1100
Centre of gravity 0.25π	rms	2.5	10	50	1.5	7.1	22
	pv	6.5	29	180	4.0	19	79
Centre of gravity 1.5π	rms	6.8	27	130	3.2	14	57
	pv	21	72	380	11	51	150
Wavelet central fringe 0.25π	rms	0.07	0.35	3.6	0.29	1.4	7.3
	pv	0.2	0.9	13	0.8	3.8	25
Wavelet central fringe 1.5π	rms	0.13	0.9	170	0.75	4.2	150
	pv	0.48	2.3	560	2.2	12	580
Wavelet envelope 0.25π	rms	1.0	5.3	53	1.6	8.7	55
	pv	3.2	15	160	5.1	23	290
Wavelet envelope 1.5π	rms	2.6	14	133	0.67	7.0	120
	pv	8.1	50	370	2.5	23	450

The upper value gives the rms error and the lower the pv value. The sampling step size is stated behind the algorithm name.
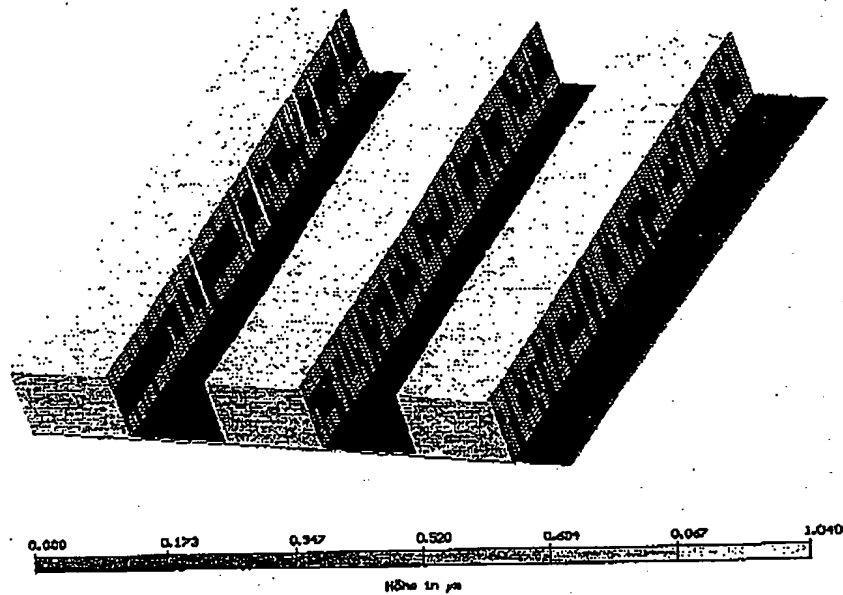
127

Fig. 5. Rectangular grating measured with the sub-Nyquist wavelet algorithm.

result we found that all algorithms are capable of an accuracy of less than 1 nm for sampling step size variations of up to ±15% which is considered sufficient for a white light interferometer. Only the algorithm which employs the centre of gravity produces a maximum error of 40 nm for sub-Nyquist signals.

In practice the vertical accuracy of a white light interferometer is mainly limited by two different kinds of noise which affect the form of the correlograms. The additive noise results from turbulence and detector noise whereas the sampling noise is caused by unwanted vibrations of the apparatus and by an inaccurate phase shift (resolution of the piezo actuator).

Synthetic correlograms with superimposed noise are generated to simulate the influence of the noise on the repeatability

$$I_i = I \cos(\Delta \Phi_i (I - n_s) + \Phi)$$

$$\times \exp\left(-\frac{(\Delta \Phi_i (I - n_s))^2}{2 w^2}\right) + n_1, \tag{15}$$

where I is the intensity, without offset; I the index within the sampling window, $I = 1, \ldots, n$; ΔS_i the sampling step size; n_s the sampling noise, Gaussian distributed; n_1 the intensity noise, Gaussian distributed.

The value of n_1 expressed in nm is used as a parameter for the sampling noise whereas the intensity noise is

quantified by the signal to noise ratio defined by

$$SNR = 2 I/n_1. \tag{16}$$

In order to determine the sensitivity to noise 200 noisy correlograms (Eq. (15)) are generated and analysed by the algorithms under test. The sampling and intensity noise are simulated separately. The rms error and the pv value of the 200 determined positions is used as a measure for the sensitivity to noise. The main results of the simulations are shown in Table 1.

Generally there is a clear proportionality of the error to the intensity noise amplitude and to the square root of the sampling rate. In the case of sampling noise it becomes more complicated because the noise is no longer additive but highly nonlinear and thus no clear dependences can be

Table 2
Measured and simulated repeatability of the white light interferometer (nm)

	rms error		pv value	
	Measured	Simulated	Measured	Simulated
Wavelet filtering 1.5π	1.5	1.2	5.6	4.5
Polynomial interpolation	2.1	1.5	8.4	5.7

128   *R.-J. Recknagel, G. Notni / Optics Communications 148 (1998) 122–128*

seen in general. Only an over proportional increase in the error for noise amplitudes greater than 50 nm can be observed which is due to the fact that the noise can be bigger than the minimal Nyquist step size.

The wavelet filtering with central fringe detection has the same characteristics as the polynomial interpolation but with significantly decreased errors. So the errors of the sub-Nyquist wavelet filtering are still lower than the ones of the polynomial interpolation with a sampling step size of 0.25π although the wavelet method needs 6 times less measured data. The wavelet filtering with envelope/central fringe detection exhibits similar characteristics as the Fourier transform with envelope/central fringe detection but is 1.5 times more insensitive to intensity noise.

4. Experiments

In order to compare the wavelet filtering to a conventional method (polynom fit) the repeatability of the measurement of the surface of a rectangular grating is determined. The grating has a high reflectivity and a highly finished surface and thus offers good conditions for the measurement of the achievable repeatability. Fig. 5 shows the measured surface.

The repeatability is found experimentally as well as theoretically by means of the simulation results. The rms- and pv-values of the repeatability are compared in Table 2.

In the experiments we used a microscopic arrangement (Leica DMR) equipped with a mirau-interferometer (40 ×). The path difference is changed by shifting the microscope table by means of a piezo actuator with a positioning accuracy of 2 nm and a shift length of 100 μm. The interferograms are recorded with an 8-bit camera by which an intensity noise of 3–4 grey levels is introduced. The camera noise, the inaccurate piezo actuator and unavoidable mechanical vibrations of the apparatus caused by external disturbances can be seen as the main reasons for random errors. The simulated results given in Table 2 are based on assumptions about the value of the intensity and sampling noise distorting the correlograms. If one assumes an effectively used dynamic range of the camera of 7 bit the SNR of the intensity noise is found to be 64. Moreover, the sampling noise is assumed to be caused only by the piezo actuator and is hence 2 nm as stated above. The topological errors corresponding to the intensity noise and the sampling noise are taken from Table 1. By adding the obtained topological errors by means of the Gauss error propagation law the resulting theoretical errors stated in Table 2 are obtained.

Although the simulation takes into account the main error sources the measured errors are slightly higher than the theoretical ones. There are two likely reasons for this. First, the sampling noise is probably higher than assumed

because it is not only caused by the piezo actuator but also by vibrations of the apparatus which have an unknown amplitude. Second, the polynomial fit is performed with a sampling step size of 0.35π and not 0.25π as it is done in the simulations. Taking these facts into consideration a good coincidence of the theoretical and experimental results is found which leads to the conclusion that all simulation results are reliable and well suited for a comparison of the presented algorithms.

5. Summary / conclusion

Several algorithms for the analysis of correlograms are presented and compared by means of computer simulations with respect to their theoretical accuracy and their sensitivity to sampling and intensity noise. Generally the proposed wavelet filtering proves to be the algorithm which is most insensitive to noise. This algorithm also has the remarkable ability to determine the centre fringe of a correlogram even if it is sub-Nyquist sampled. Additionally, in the case of sub-Nyquist sampling the algorithm is not only less sensitive to noise than the polynomial interpolation (sampled with 0.25π) but needs 6 times less measured data. Furthermore, the systematic error caused by the algorithms themselves is always below 1 nm.

Considering the computational cost the wavelet filtering and Fourier transform method are probably at the same level provided the same degree of optimisation, i.e. not calculating a whole FFT and a good estimation of the maximum position and integer arithmetic in the case of the wavelet filtering. Experimentally an achievable rms repeatability of 1.5 nm is determined for sub-Nyquist wavelet filtering.

References

[1] P. de Groot, L. Deck, Optics Lett. 18 (1993) 1462.
[2] P. de Groot, L. Deck, J. Mod. Optics 42 (1995) 389.
[3] R. Dändliker, E. Zimmermann, G. Frosio, Optics Lett. 17 (1992) 679.
[4] P.J. Caber, Appl. Optics 32 (1993) 3438.
[5] G.S. Kino, S.C. Chim, Appl. Optics 29 (1990) 3775.
[6] K.G. Larkin, J.Opt. Soc. Am. A 13 (1996) 832.
[7] R.-J. Recknagel, Diploma work, Friedrich-Schiller-University Jena, 1996.
[8] M. Itoh et al., Opt. Rev. 2 (1995) 135.
[9] T. Dresel, G. Haeusler, H. Venzke, Appl. Optics 31 (1992) 919.
[10] P. Sandoz, J. Mod. Optics 43 (1996) 1545.
[11] I. Daubechies, Ten Lectures on Wavelets, Society for Industrial and Applied Mathematics, Philadelphia, PA, 1992.
[12] A. Bruce, H.-Y. Gao, S+Wavelets User's Manual Version 1.0, Seattle StatSci, MathSoft Inc., 1994.

4 Practical Aspects of STM and AFM Measurements

At present the STM and AFM imaging of samples with relatively flat surfaces is a routine task. However, more elaborate efforts are required to obtain the reliable images needed for thorough characterization of the surfaces. Therefore, in carrying out STM and AFM measurements, one should optimize the experimental conditions and consider the possibility of image artifacts having various different origins. Several practical aspects of STM and AFM experiments are discussed in this chapter.

4.1 Samples

The application of electron and optical microscopy methods often requires elaborate sample preparations and measurements in special environments. In this respect, the scanning probe techniques (especially AFM) are more universal and can be applied to a broad range of samples in different environments. The use of atomic force microscopes is mostly limited by the roughness of samples. Because commercial AFM probes have a height of several microns, samples with surface corrugations below 1 μm can be investigated with atomic force microscopes. With scanning tunneling microscopes, one can study surfaces with larger corrugations using longer tips. However, very long STM tips cannot be employed because of their mechanical instability during scanning. Also, surfaces with extremely sharp features cannot be properly examined with STM and AFM because they lead to image artifacts (see Section 4.3.3).

As for the size of the surface area to be imaged, there is no practical limit. Silicon wafers ca. 10 cm in diameter and microcrystals with dimensions in the micron range can be examined with scanning tunneling and atomic force microscopes. Using an optical microscope or an optical camera, each of which is commonly combined with a scanning probe microscope, one can position the probe in the area of interest and examine, for example, the same area of a conducting sample, successively with STM and AFM. This is better realized by using a large-scale scanner, which can cover areas greater than 15 μm × 15 μm and provide atomic-scale imaging.

STM and AFM experiments can be conducted in different environments (e.g., UHV, ambient conditions, under liquid, electrochemical medium) and at temperatures ranging from the liquid helium temperature up to several hundreds of degrees Celsius. To study samples under liquid or in an electrochemical medium one can use appropriate cells supplied with commercial STM and AFM instruments. In air, many metal and semiconductor surfaces are covered with an oxide layer, which prevents

their examination in ambient conditions. Usually these materials are examined in UHV, and before measurement their surfaces are subjected to cleaning procedures. Recently, it was demonstrated that the oxide overlayers of semiconductors GaAs and silicon can be etched away in an electrochemical environment. Therefore, in-situ STM measurements in electrochemical cells make it possible to examine the clean surfaces of these semiconductors on an atomic scale [1]. Metallic and semiconducting materials stable to oxidation can be studied in ambient conditions.

It is natural to ask what minimum electrical conductivity a sample must have, to be examined by STM. Samples with bulk electrical conductivity as low as 10^{-9} S/cm can be examined with conventional STM instruments. If a sample has low conductivity, the electrical contact between the sample surface and its holder should be improved by applying silver or gold paste, and the tip should be positioned close to the contact. The development of low-current STM instrumentation allows the measurements of poorly conducting materials with I_{set} in the picoamp (pA) range and R_{gap} up to teraohms (TΩ).

4.2   Optimization of Experiments

To extract comprehensive physico-chemical information about the surface under examination, the experimental conditions need to be optimized. It is desirable first to image the sample with minimal tip–sample force interactions and then to vary the experimental parameters systematically to examine their influence on the image. This approach provides information that is useful for the image interpretation.

4.2.1   Optimization of STM Experiments

When the sample's electrical conductivity characteristics are known or determined by measuring the I–V dependence, one can estimate the tunneling parameters appropriate for the STM imaging. The choice of the bias voltage polarity is not crucial for metallic samples, but it is essential for semiconducting materials. To understand properly the nature of the STM images of semiconductors, it is necessary to examine their dependence on the magnitude and polarity of the bias voltage. In addition, one should consider a possible complication related to the bending of the valence and conduction bands due to the bias voltage (see Chapter 5). This band bending can alter electron occupation at the top of the valence band and at the bottom of the conduction band. This strongly influences the STM images, depending on the magnitude and the sign of the bias voltage.

To minimize the tip–sample force interaction in the imaging of metallic samples, an initial scan should be performed with high gap resistance (e. g., by using a small set-point current below 1 nA and a relatively high bias voltage around 1–2 V). Scan-

ning with high gap resistance is likely to produce images with low signal-to-noise ratio. Then a gradual decrease in the gap resistance, which is equivalent to decreasing the tip–sample distance, can lead to better-resolved images. However, the increase of the tip–sample force interactions at small tip–sample distances might lead to image variation and even to surface etching.

In STM and AFM of layered compounds (e.g., transition-metal dichalcogenides and organic conducting salts), molecular adsorbates, and polymers [2–5], etching of the surface layers is frequently observed. Figure 4.1 shows the image changes associ-
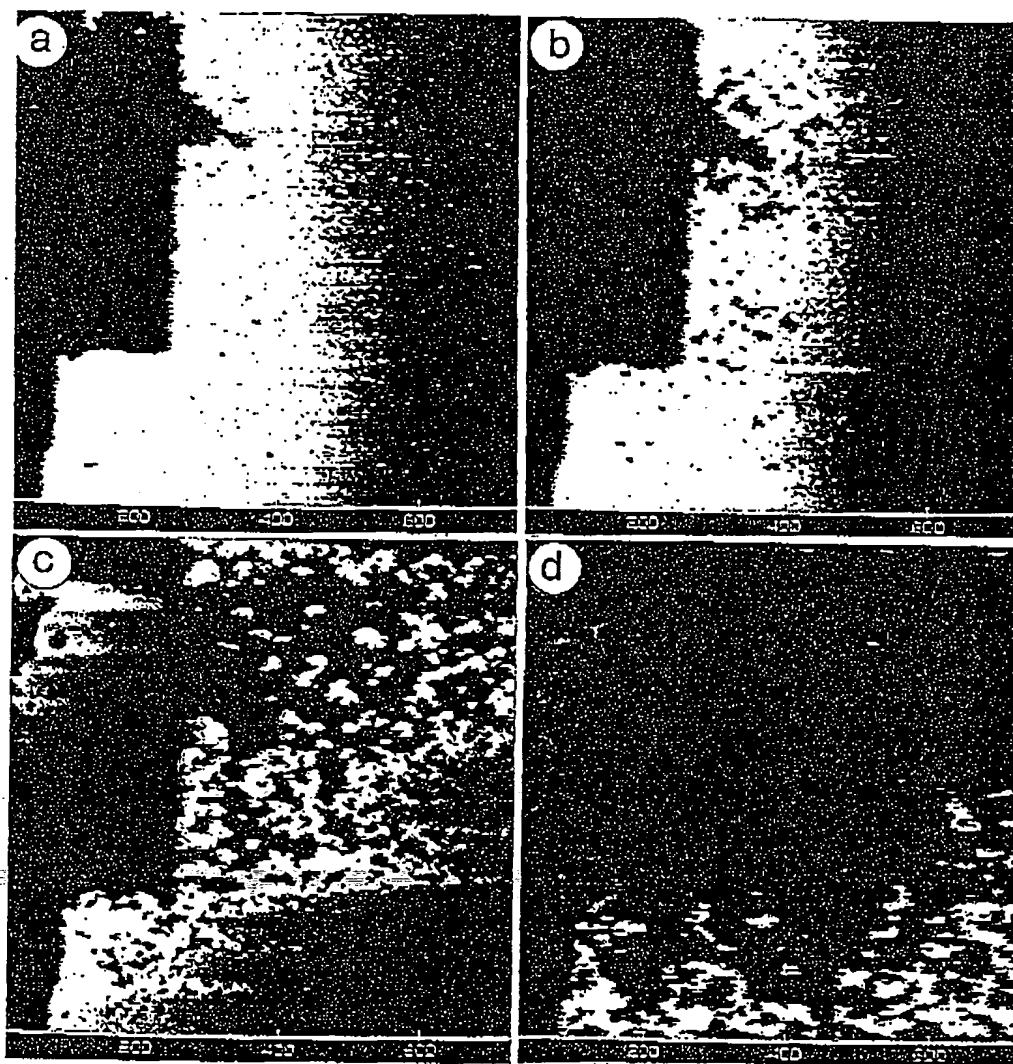
Figure 4.1 (a)–(d) Four successive STM height images of the organic conducting salt α-(BEDT-TTF)$_2$I$_3$ (I_{set} = 1 nA, V_{bias} = 0.1 V). The contrast covers height variations in the 0–10 nm range.

50   *4 Practical Aspects of STM and AFM Measurements*

ated with etching on the surface of an organic conductor, which were recorded in successive scans. These images reveal a gradual removal of the topmost layer and a growth of surface holes in the lower-lying layer. Crystalline surfaces with a large number of steps, holes, and other structural imperfections are extensively etched during STM and AFM measurements. The etching proceeds faster at high applied force in AFM, and at small gap resistance in STM. The etching speed also increases when the tip spends more time in a particular area of the surface and when the surface steps are oriented perpendicular to the fast-scanning direction. In STM of organic conducting salts, not only surface etching but also surface growth can occasionally be observed (see Chapter 10). In atomic-scale STM and AFM imaging of layered crystals, layer removal by etching is seen as the successive disappearance and appearance of the periodic image patterns. The results of etching can be recognized by zooming out of the scanned area. In general, the etching mechanism in STM and AFM is not well understood, but its essential features can be rationalized in terms of the tip–sample force interactions. In STM it is also possible that electric field-related effects are involved in the etching process [2].

4.2.2 Optimization of Contact-mode AFM Experiments

In optimizing AFM experiments, it is important to adjust the level of the set-point force, which determines the force applied to the sample (i. e., the operational force, F_{opr}). This can be done by using the force-vs.-distance curve. As an example, Figs. 4.2 (a)–4.2 (c) show such curves recorded on a polyethylene tape in air and in water. These curves are obtained by plotting the cantilever deflection (ΔD) from its rest position ($\Delta D = 0$) as a function of the z-position of the sample. The force-vs.-distance curve is obtained by converting the cantilever displacement into the force unit according to the relationship $F = k_{cl} \Delta D$, where k_{cl} is the spring constant of the free cantilever. The total force experienced by the cantilever is repulsive in the region of $\Delta D > 0$ ($F > 0$), and attractive in the region of $\Delta D < 0$ ($F < 0$).

A strong hysteresis is commonly observed in the ambient-condition experiment due to the capillary force (F_{cap}) associated with the surface contamination layer (Figs. 4.2 (a) and 4.2 (b)). For converting the cantilever displacement ΔD to the force involved, it is convenient to redefine the pull-out force ($F_{pull-out}$) as the force corresponding to the minimum point of the retrieval curve, so that $F_{pull-out}$ is represented as a negative number in Figs. 4.2 (a) and 4.2 (b). When the cantilever is bent up to reach the set-point deflection, ΔD_{set} (or equivalently the set-point force, $F_{set} = k_{cl} \Delta D_{set}$), the operational force is given by $F_{opr} = F_{set} - F_{pull-out}$. When the tip–sample adhesion is negligible, $F_{pull-out}$ is approximately equal to the capillary force F_{cap}, which is typically higher than 10 nN in magnitude [6]. It is estimated that forces from tens to hundreds of nanonewtons are applied to the sample surface in ambient-condition experiments [7]. As a result, the tip with an apex radius of several nanometers
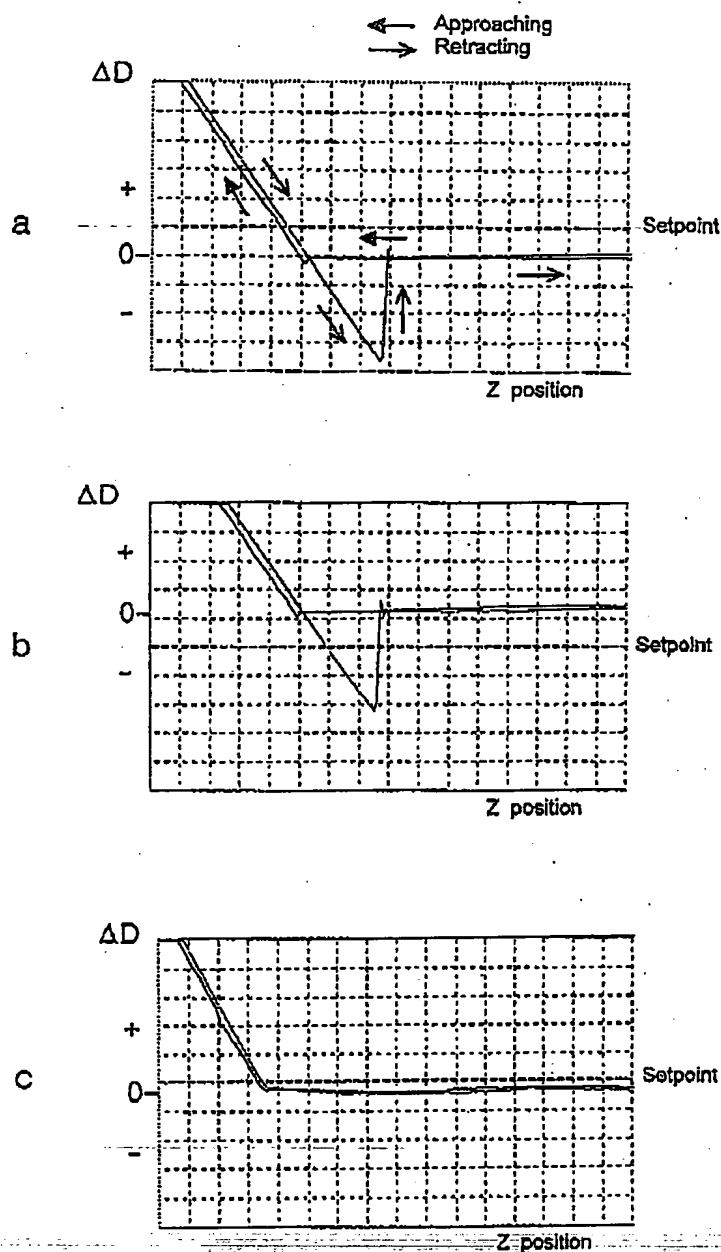
Figure 4.2 Force-vs.-distance curves determined for a polyethylene tape: (a), (b) in air; (c) under water. The arrows indicate the direction of the sample's approach to and retrieval from the tip. The cantilever deflection ΔD, plotted as the vertical axis, is converted into the force unit by the relationship $F = k_{cl} \Delta D$, where k_{cl} is the spring constant of the free cantilever. The set-point deflection ΔD_{set} is indicated by the broken line.

52   4 *Practical Aspects of STM and AFM Measurements*

will produce a load of several gigapascals (GPa), which might lead to irreversible surface modification of soft materials such as polymers. A nondestructive imaging of polymers requires the application of smaller forces (a few nanonewtons or less).

It is clear from the above that by adjusting the set-point level, the user can image sample surfaces with different applied forces. By raising the set-point level, high-force imaging can be carried out. To minimize the operational force, one can adjust the set-point level close to the jump-out point (Fig. 4.2 (b)). In this case, the net force acting on the cantilever is attractive (i.e., the cantilever is bent down), but the image contrast is determined by the variation of the repulsive force between the sample and tip. Due to the cantilever instability near the jump-out point, however, a stable operation is achieved only when the set-point force is not close to $F_{pull-out}$ [7a]. Therefore, in ambient-condition AFM measurements, a part of the capillary force should be overcome by the repulsive force. A more substantial drop in the applied force is achieved in subliquid measurements. In the absence of the capillary force and the related hysteresis in the force-vs.-distance curve, the operational force can be diminished to subnanonewton range by adjusting the set-point close to the tip–sample disconnection point (Fig. 4.2 (c)). In such a case, the operational force can be reduced to the subnanonewton range by using soft cantilevers with spring constants smaller than ca. 0.06 N/m [7a].
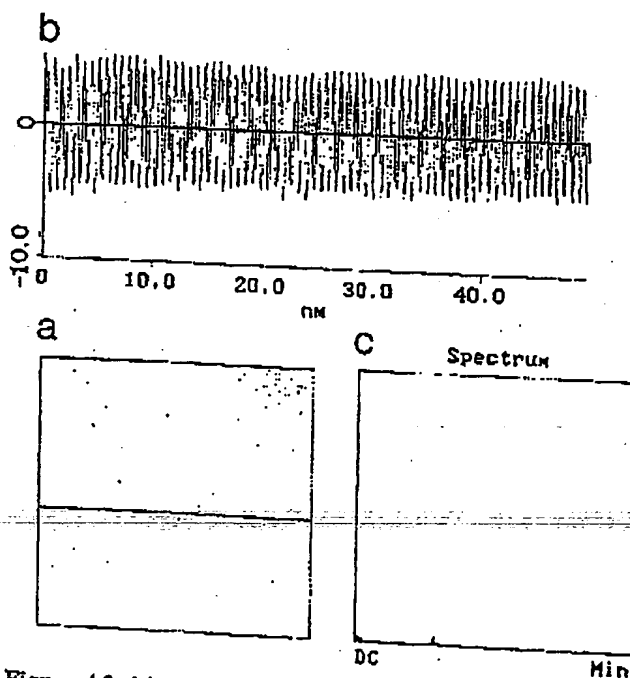

Figure 4.3 (a) Contact-mode AFM image recorded under water with a feedback gain high enough to cause the cantilever to vibrate. (b) Cross-section profile along the x-direction of the image in (a). (c) FFT power spectrum of the cross-section profile in (b).

For studies of soft materials, cantilevers with small spring constants are needed. To find soft ones among a batch of commercial cantilevers with different spring constants, one can determine their resonance frequencies by performing AFM experiments under water [8]. Scanning with a very high feedback gain causes the cantilever to vibrate, thereby leading to a characteristic oscillation image (Fig. 4.3 (a)). The FFT power spectrum of the horizontal cross-section profile of this image exhibits a pronounced peak at the frequency of the cantilever (Figs. 4.3 (b) and 4.3 (c)). This frequency is very close to that of the free cantilever, due to the weak tip-sample coupling under water.

The effect of the applied force on the resolution of AFM images is illustrated in Fig. 4.4, which shows the images of a stretched polyethylene tape recorded in air and under water with the same tip. In subwater measurements, where the operational force is smaller than that in air, the tip-sample contact area is smaller. This improves the lateral resolution significantly; the width of the nanofibrils measured in the experiments under water (15-25 nm) is smaller than that determined from the image recorded in air by a factor of at least two [9].
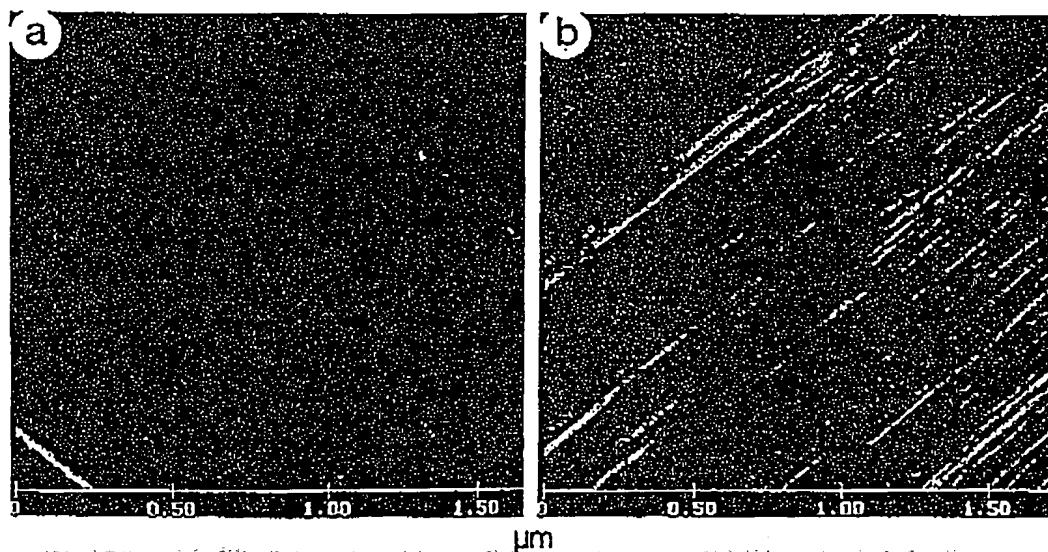

Figure 4.4 AFM height images of a stretched polyethylene tape measured with the same cantilever (a) in air and (b) under water. The contrast covers height variations in the 0–10 nm range.

4.2.3 Optimization of Tapping-Mode AFM Experiments

For soft materials such as polymers and biological compounds, the application of even the smallest force in the contact-mode AFM mode might damage the weak surface structures. One of the factors causing this problem is the lateral force that the

54   4 *Practical Aspects of STM and AFM Measurements*

tip applies to the sample surface. To avoid this lateral force, one can employ tapping-mode AFM in air or under liquid. Currently, this mode is more widely applied in AFM studies of soft materials than other modulation techniques. However, several aspects of the tapping mode are yet to be clarified. The most important questions are the range of the compressive forces experienced by the sample in this experiment, and the image resolution that can be achieved.

By using the tapping mode under water, one can substantially diminish the amplitude of the cantilever vibration in the free position compared with the corresponding amplitude in air. In this way, tip–sample force interaction can be reduced to a level lower than that reached in the contact mode under water [8]. In subwater imaging with the tapping mode, surface nanofibrils of 2–3 nm in diameter were recorded on a stretched polyethylene tape. The skin layer made up of these nanofibrils was less damaged in the tapping-mode operation than in the contact-mode measurements with ca. 1 nN force. Consequently, the compressive forces applied to the sample in the tapping-mode measurements were effectively smaller than 1 nN. Other estimates suggest that this force is around 0.4 nN [10].

The applicability of the tapping mode to atomic-scale imaging is not clear. In tapping-mode imaging of layered semiconductor WSe_2, the atomic-scale pattern of the surface lattice was detected (Fig. 4.5). The signal-to-noise ratio of this image is inferior to that of the contact-mode image obtained with the same tip in the same place on the sample. In the tapping mode, atomic-scale images are observed occasionally,
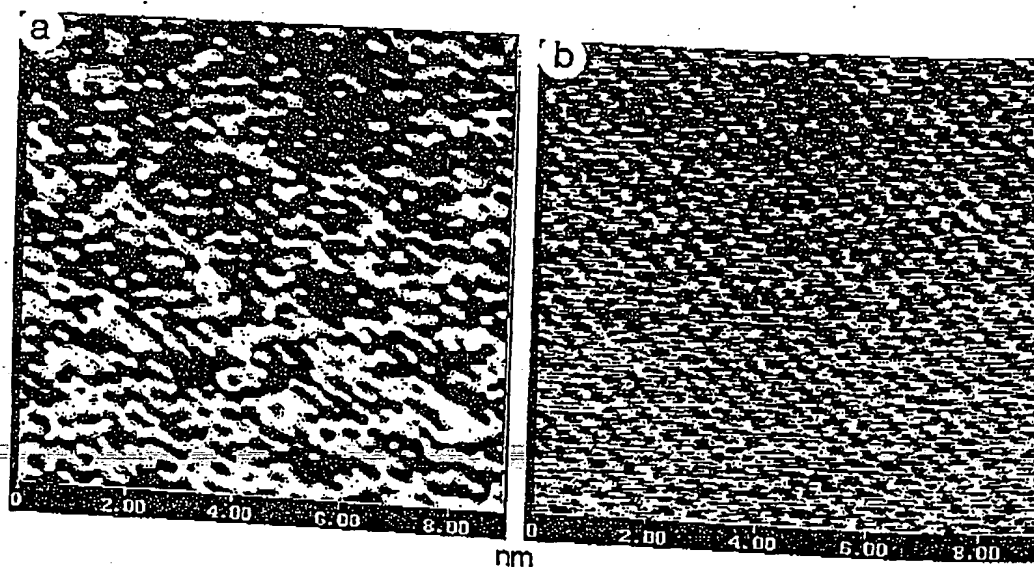

Figure 4.5 (a) Tapping-mode AFM height image of layered compound WSe_2. (b) Contact-mode AFM height image obtained with the same tip and in the same place on the WSe_2 crystal. The contrast covers height variations in the 0.0–0.3 nm range in (a), and in the 0.0–0.5 nm range in (b).

so it is difficult to establish their origin. Such imaging may be caused by a small lateral-force component that the tip experiences during the tapping. The latter is possible because the cantilever in the rest position is slightly inclined to the sample surface, as pointed out in Section 3.3.1.

4.3 STM and AFM Measurements

Several aspects of STM and AFM imaging on different scales are summarized in this section. The specific features of imaging that depend on the nature of the compounds under consideration will be described in later chapters.

4.3.1 Large-Scale Imaging

To examine a sample by STM and AFM, it is preferable to start with large-scale imaging. In general, images of areas larger than 100 nm × 100 nm do not provide information about the contrast variation within a unit cell. However, they contain invaluable data about the topography of the samples and other surface properties (e.g., hardness, friction). The images of amorphous materials such as polymers exhibit different types of surface morphology (for details, see Chapter 12). Flat terraces separated by single or multiple steps are typically found on the surfaces of crystalline samples and thin organic layers adsorbed on substrates. The step heights in the nanometer and angstrom range are rather difficult to measure by physical methods other than STM and AFM. Knowledge of the surface topography obtained with large-scale imaging also allows one to select a flatter and less defective region of the surface for atomic-scale imaging. In some cases, perfect surface layers can be prepared by deliberately etching away the defective topmost layers with the scanning tip.

When surfaces contain chemical and structural defects such as vacancies, dopants, and noncrystalline domains, large-scale STM images should be analyzed with care because they can be dominated by the electronic structures associated with the defects. When defective features are found in the images, it is important to check how the image contrast is influenced by the polarity of the bias voltage. This check can help identify the nature of the defects because, depending on the bias voltage polarity, different electronic states of the sample may become involved in the tunneling process (see Chapter 7). The STM images of defects may be influenced by tip–sample force interactions, and these effects can be observed in the large-scale as well in the atomic-scale images. For instance, in the STM study of defects in layered semiconductor WSe_2, the nanometer-scale bright spots at high R_{gap} are reversibly converted to bright rings at low R_{gap} (Fig. 4.6) [11]. The nanometer-scale bright spot is assigned to the trapped electron state around a donor dopant on the surface Se-atom
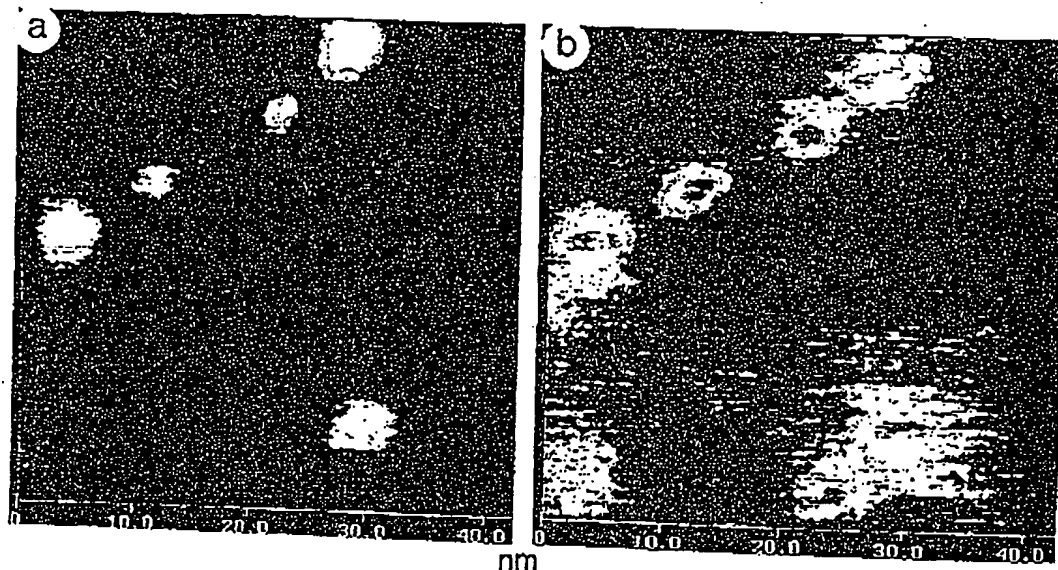
56   *4 Practical Aspects of STM and AFM Measurements*

nm

Figure 4.6 STM height images of WSe$_2$ (a) I_{set} = 1 nA and V_{bias} = −0.73 V; (b) I_{set} = 1 nA, V_{bias} = −0.5 V. The contrast covers height variations in the 0–1 nm range.

sheet, and this spot becomes a ring because the trapped electron around the dopant atom becomes freed when the ring center is compressed by the tip. Thus, it is also important to examine the image variations at different R_{gap} values.

The interpretation of large-scale AFM images can be complicated when chemically or structurally different domains are present on the surface, because they might modify the local hardness and friction of the surface. This leads to more complicated image patterns than those expected from the surface topography. To confirm the surface-hardness contribution to the images, it is necessary to conduct force-dependent measurements by varying the set-point force level, since the image contrast between the hard and soft regions of the surface increases with increasing load. The softer region of a surface is expected to be more depressed by the tip force, which increases the tip–sample contact area. This will enhance the lateral force (i. e., frictional force) that acts on the tip in the softer region of the surface, which will be manifest in the LFM images.

In principle, it should be possible to distinguish chemically different surface domains by utilizing the response of the AFM probe to the hardness, friction and different surface forces of a sample surface. In most cases, however, interpretation of the associated image contrast is not straightforward, because the surface hardness and friction are affected both by chemical structures and by their packing arrangements. In addition, hydrophilic and hydrophobic surface domains can be different in their mechanical properties. To deconvolute the different factors contributing to the images, it would be useful to employ various chemically modified tips to emphasize, and thus identify, specific types of tip–sample interactions [12].

4.3.2 Atomic-Scale Imaging

STM and AFM images obtained for small areas (below 100 nm × 100 nm) of crystal-line surfaces exhibit molecular- and atomic-scale features. Currently, one can obtain atomic-scale AFM images with a signal-to-noise ratio comparable with that found for atomic-scale STM images. For compounds with known crystal structures, the im-ages of the crystal faces are compared with the lattices expected from the bulk crystal data. Therefore, it is important to determine reliably the surface unit cells of the im-ages. To minimize the effect of the thermal drift on the geometrical parameters of the images, it is necessary to carry out imaging after thermal equilibrium has been reached between the sample and microscope stage, and to conduct measurements with high scanning speed. Further, the images should be collected in the "up" and "down" scanning directions and at different rotation angles of the fast-scanning di-rection. Finally, the geometrical parameters of these measurements should be aver-aged. This procedure gives rise to more reliable surface unit-cell parameters from the images. For layered compounds the image and crystallographic lattice parameters are in agreement, typically to an accuracy of within 5%.

In STM and AFM studies it is common to observe variations of the image details in atomic-scale patterns depending on the experimental conditions. Image variation may occur spontaneously due the instability of the tip and the surface, even when the scanning is carried out without changing the experimental conditions. Alterna-tively, image variation may reflect a change in the tip–sample distance and applied force, so it can help to characterize the sample surface. For example, the STM images of some organic conducting salts exhibit an image variation as a function of R_{gap} (see Chapter 10). Such a variation may originate from tip–sample force interaction, the effect of which on the surface structure can be directly observed in the AFM im-ages. To understand the dependence of the image features on the applied force, it is necessary to carry out systematic force-dependent measurements. Figure 4.7 shows the results of force-dependent AFM experiments for the layered telluride $NbGe_{3/7}Te_2$. These images show bright spots corresponding to surface Te atoms. The low-force AFM image exhibits the hexagonal pattern expected from the atomic arrangement of the Te-atom surface layer. In the high-force image, periodic rows of depressed surface atoms appear; upon reducing the applied force, this feature disap-pears. These reversible image changes show the occurrence of reversible, atomic-scale surface relaxation. As will be discussed in Chapter 9, the depressed atoms are associ-ated with those Te atoms on the surface whose local hardness is small [13]. Thus, the high-force image reveals the variation of the surface local hardness, and the force-dependent AFM studies provide an experimental basis for nanomechanics.

As already mentioned, the images of inorganic layered compounds obtained in high-force experiments exhibit a high signal-to-noise ratio. Furthermore, atomic-size imperfections were found in high-force images of $TaGe_{0.355}Te_2$. Figure 4.8 shows four successive images of $TaGe_{0.355}Te_2$, with two imperfections indicated with ar-
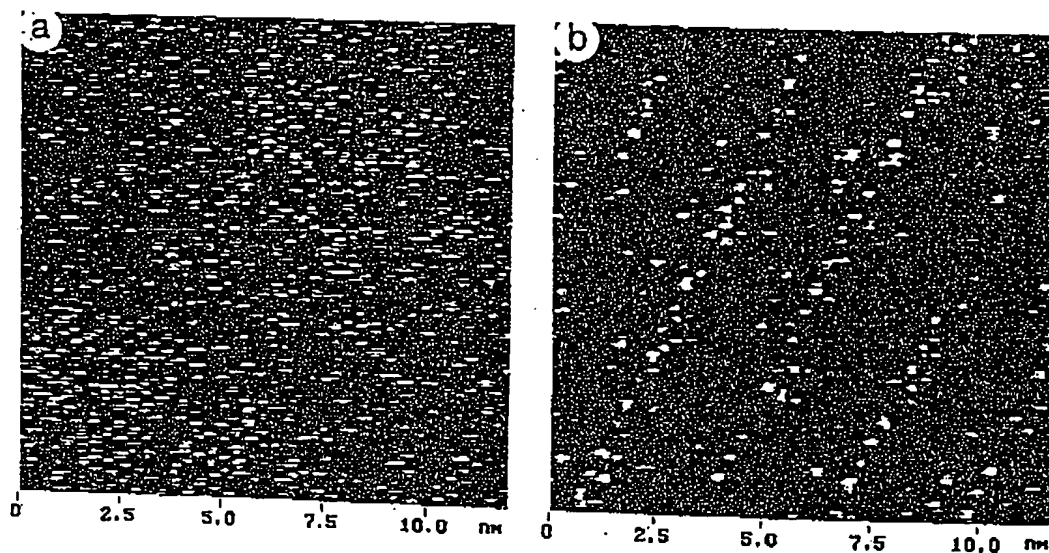
58   *4 Practical Aspects of STM and AFM Measurements*

Figure 4.7 AFM height images of $NbGe_{3/7}Te_2$ recorded with (a) 170 nN and (b) 270 nN. The contrast covers height variations in the 0–1 nm range.

rows. The defects have brighter and darker contrasts compared with their neighbors in the rows. The cross-section profiles along these rows show these contrast differences in all four successive images. The atomic-size defects change their positions in the images due to thermal drift, but the distance between them remains constant. These findings imply that under high applied forces the tip–sample interactions may lead to an "effective sharpening" of the tip.

In AFM studies of crystalline surfaces, one can obtain LFM images of well-resolved atomic-scale patterns. As measurements of such patterns are useful in answering several questions concerning the atomic origin of friction, the examination of atomic-scale LFM images is necessary. Currently, various aspects of atomic-scale friction are being studied intensively [14].

4.3.3 Image Artifacts

The occurrence of artifacts in STM and AFM images has been a bothersome problem since the invention of scanning probe techniques [15, 16]. Striking image artifacts are often observed for a hard surface with steep corrugations. If a sample surface has structural features sharper than the tip apex, the imaging roles of the tip and surface are reversed so that the tip shape appears in the image. For example, the AFM imaging of a fractured surface of a carbon fiber (about 10 μm in diameter), which contains numerous needles and sharp edges of graphite planes, might result in an image showing the shape of the Si_3N_4 tip (Fig. 4.9) [17]. This example shows
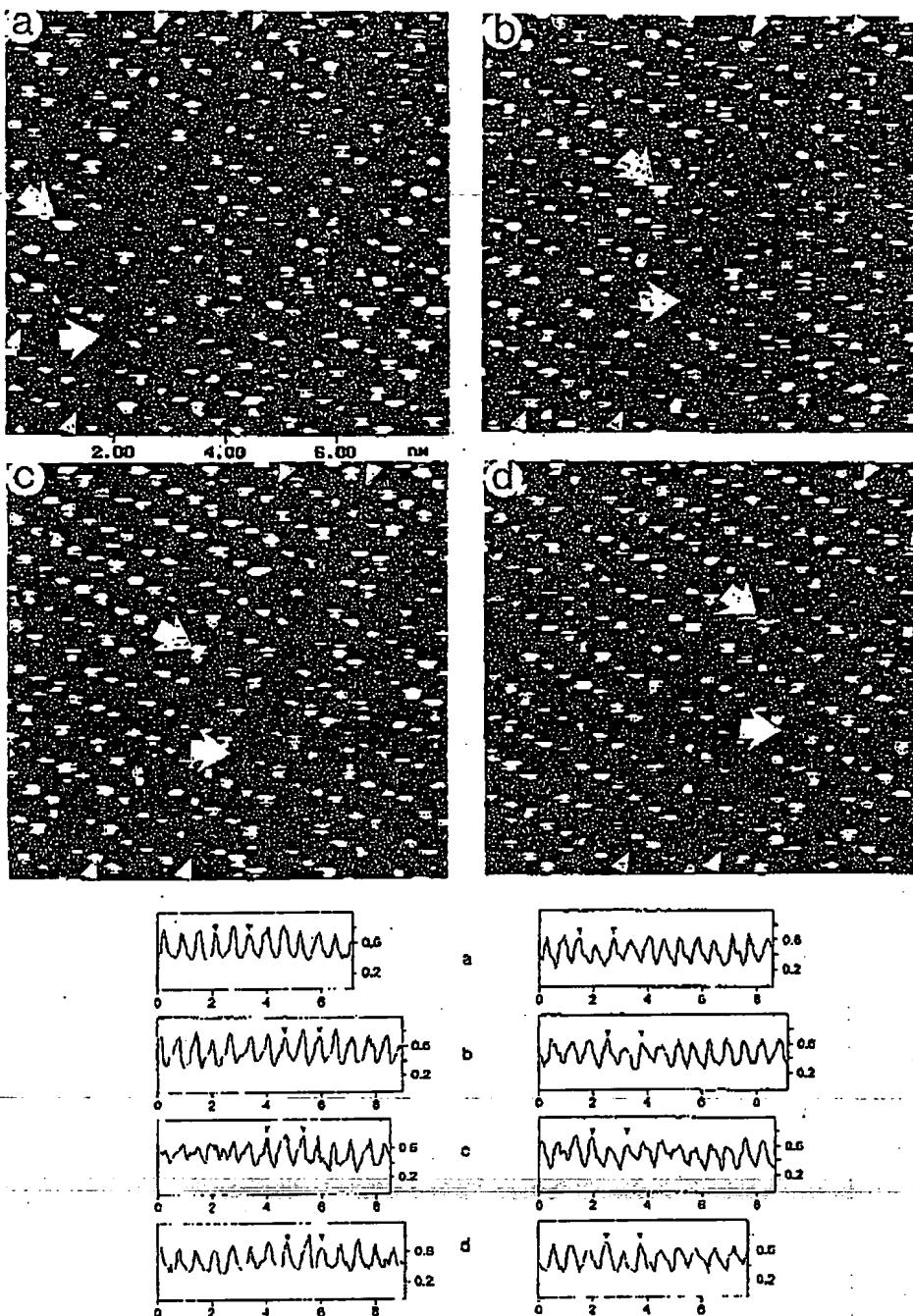
Figure 4.8 (a)–(d) Sequence of four contact-mode AFM height images of $TaGe_{0.355}Te_2$ recorded at 10 s intervals with high applied force. The contrast covers height variations in the 0.0–0.7 nm range. The large arrows point to the atomic-size defects. The rows containing the defects are indicated by small wedges, and the height profiles along these rows are shown below the images.

60   *4 Practical Aspects of STM and AFM Measurements*

a definite limitation of STM and AFM in studying such surfaces. For flat surfaces, image imperfections might occur due to a multiple-tip effect and tip asymmetry. The image features associated with double-tip imaging are characterized by "ghost" patterns, in which the surface features are repeated. As an example, Fig. 4.9 (b) shows the AFM image of the supramolecular structure of an organic amphiphile (see Chapter 12).
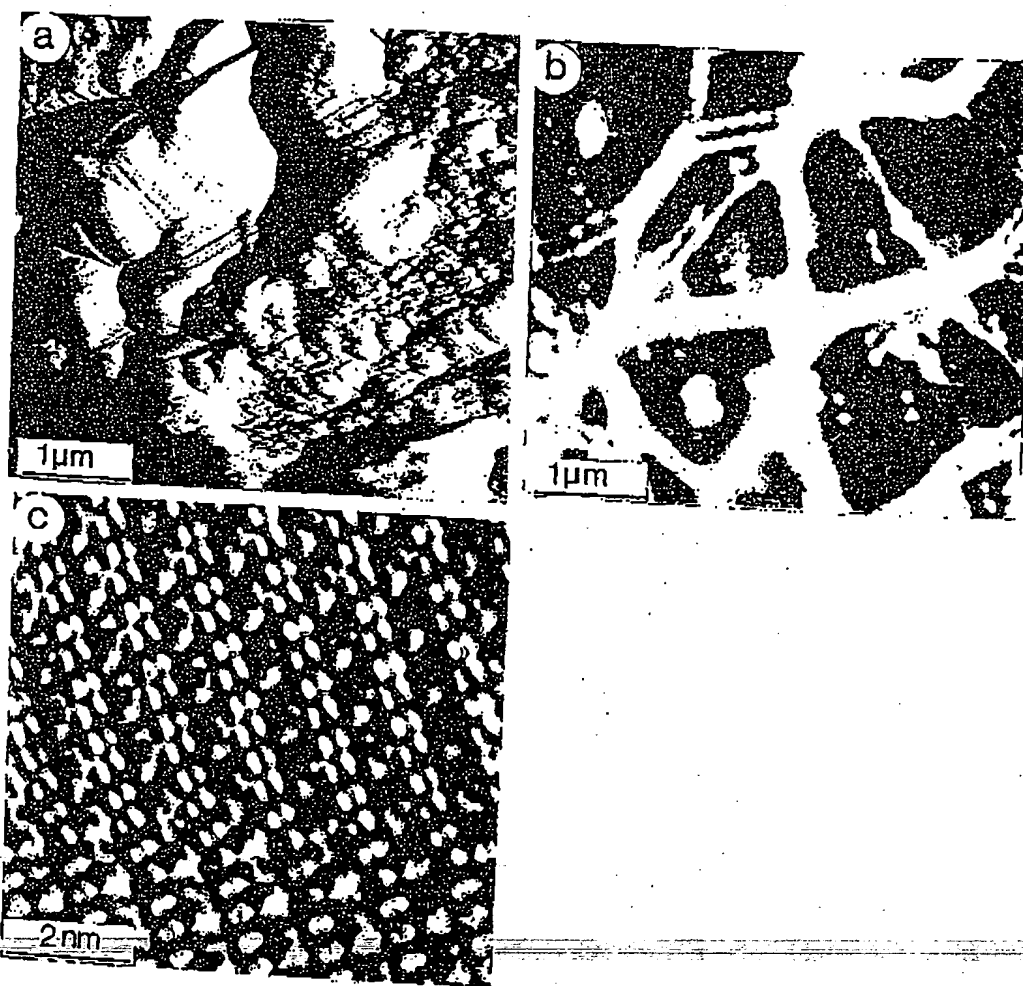

Figure 4.9 (a) Contact-mode AFM force image recorded on a fractured surface of a carbon fiber. The pyramidal-shape pattern in the upper left-hand corner shows the shape of the probing tip. The contrast covers force variations in relative units. (b) AFM height image of the adsorbate of organic amphiphile 10MS (see Chapter 12). The contrast covers height variations in the 0–90 nm range. (c) STM height image of organic conducting salt α-(BEDT-TTF)$_2$I$_3$ (I_{set} = 3.5 nA, V_{bias} = 88.5 mV). The contrast covers height variations in the 0–1 nm range.

It is worthwhile to comment on the surface imperfections of highly ordered pyrolytic graphite (HOPG), samples of which are used as a substrate for depositing organic molecules for their STM imaging. Despite its flat terraces, STM images of HOPG occasionally exhibit disordered and partially ordered features of different shapes, which occur at the surface steps and grain boundaries [18]. Therefore, in experiments with biological and organic molecules adsorbed on graphite, it is necessary to distinguish between the features of defective graphite and those of adsorbed molecules.

Typical artifacts that occur in atomic-scale STM images are shown in Fig. 4.9 (c). A sudden change happens in the center of the image, and the periodic features in the lower and upper parts have different contrasts. Such variations might occur during scanning, due to a spontaneous change in the tip and in the tip–sample gap. In some cases, such changes are accompanied by a small shift of the periodic features in different parts of the image. This can happen when the atoms located in different places on the tip apex become involved in tunneling over different places on the sample surface. The drastic pattern changes observed during an STM study of an Si(111) 7×7 surface in UHV [19] were explained by the sudden change in the electronic states of the tip participating in the tunneling.

Another kind of multiple-tip effect is observed in STM images of HOPG [20]. For example, Fig. 4.10 (a) shows an image of HOPG containing two regions (I and II) with different crystallographic orientations. The angle of misalignment is about 40°. The border region III shows a pattern (Fig. 4.10 (b)) which resembles the superposition of the images of the domains I and II. Such images can be explained if the current is collected simultaneously from the two regions by two microtips [20]. It should be noted that the occurrence of STM images with superstructure patterns is not always caused by tip-related artifacts. For example, such images can arise from misalignment of a surface layer of graphite with respect to the underlying graphite lattice (see Chapter 9).

The atomic-scale image imperfections resulting from nonideal tip geometry are best illustrated by those found for HOPG. Mizes et al [21] simulated the anomalous images of HOPG by the superposition of three sine waves, whose amplitude and phases were adjusted to match the experimental data. A multiple-tip effect in the HOPG image has been also considered by Colton et al. [22]. Their results suggest that the image distortion is caused more strongly by the tip asymmetry than by the number of tip atoms. The same conclusion was reached by Ren et al. [23], who calculated the partial electron density plots for layered compounds β-Nb_3I_8 and WTe_2 with two- and three-atom tips of different geometry.

Many image artifacts are not self-evident, so one should carry out repeated (though tedious) measurements to characterize properly the sample under examination. For large-scale measurements of corrugated surfaces, sharp tips are desirable; it is therefore useful to test the tip shape with standard samples of known profiles (see Section 3.4.2). However, this does not totally eliminate image artifacts, because
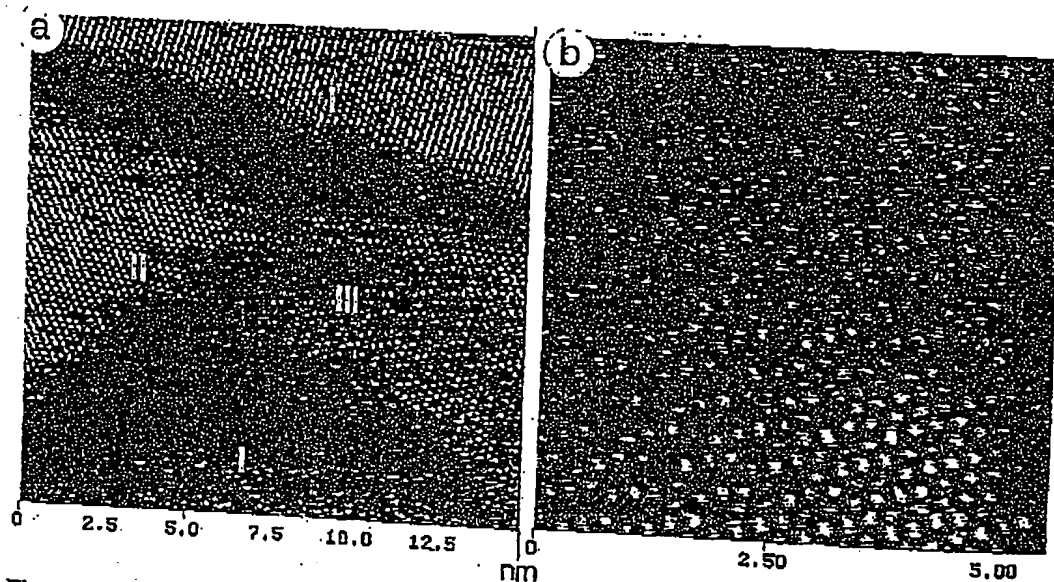
62   4 *Practical Aspects of STM and AFM Measurements*

Figure 4.10 (a) STM current image of a defective region of HOPG (I_{set} = 1 nA, V_{bias} = 1 mV), where surface domains with different patterns are indicated with labels I–III. (b) STM current image recorded within the domain III. The contrast is proportional to current variations in relative units. (Courtesy of C. Wang)

a selected tip can be modified during the scanning. Therefore, in the absence of a reliable control of the tip apex geometry, it is common to employ several different tips for the examination of a given surface and to choose the most reproducible images as the genuine representations of the sample under consideration. In this process, one can take the advantage of the expected symmetry of the surface. For highly symmetrical surfaces, the most characteristic atomic-scale images are likely to be highly symmetrical ones.

References

[1] K. Itaya, R. Sugawara, Y. Morita, H. Tokumoto, *Appl. Phys. Lett.* 1992, *60*, 2534.
[2] (a) B. A. Parkinson, *J. Am. Chem. Soc.* 1990, *112*, 7498. (b) E. Delawski, B. A. Parkinson, *J. Am. Chem. Soc.* 1992, *114*, 1661. (c) Y. Kim, C. M. Lieber, *Science* 1992, *257*, 375.
[3] S. N. Magonov, A. Ya. Gorenberg, G. Bar, H.-J. Cantow, E. B. Yagubskii, *Adv. Mater.* 1993, *5*, 453.
[4] A. Wawkuschewski, H.-J. Cantow, S. N. Magonov, *Langmuir* 1993, *9*, 2778.
[5] O. M. Leung, M. C. Goh, *Science* 1992, *255*, 64.
[6] C. M. Mate, M. R. Lorenz, V. I. Novotny, *J. Chem. Phys.* 1989, *90*, 7550.

[7] (a) A. L. Weisenhorn, P. K. Hansma, T. R. Albrecht, C. F. Quate, *Appl. Phys. Lett.* 1989, *54*, 2651. (b) A. L. Weisenhorn, P. Maivald, H.-J. Butt, P. K. Hansma, *Phys. Rev. B* 1992, *45*, 11226.

[8] A. Wawkuschewski, K. Crämer, H.-J. Cantow, S. N. Magonov, *Ultramicroscopy* 1995, *58*, 185.

[9] A. Wawkuschewski, H.-J. Cantow, S. N. Magonov, S. Sheiko, M. Möller, *Polym. Bull.* 1993, *31*, 693.

[10] M. Radmacher, M. Fritz, P. K. Hansma, *Science* 1994, *265*, 1577.

[11] S. N. Magonov, H.-J. Cantow, M.-H. Whangbo, *Surf. Sci. Lett.* 1994, *318*, L1175.

[12] V. T. Moy, E.-L. Florin, H. E. Gaub, *Colloid. Surf.* 1994, *93*, 343.

[13] (a) H. Bengel, H.-J. Cantow, S. N. Magonov, L. Monconduit, M. Evain, M.-H. Whangbo, *Surf. Sci. Lett.* 1994, *321*, L170. (b) H. Bengel, H.-J. Cantow, S. N. Magonov, L. Monconduit, M. Evain, W. Liang, M.-H. Whangbo, *Adv. Mater.* 1994, *6*, 649.

[14] H.-J. Günterodt, D. Anselmetti, E. Meyer (Eds.), *Forces in Scanning Probe Methods*, Kluwer, Dordrecht, 1995.

[15] (a) D. Nyyssonen, L. Landstein, E. Coombs, *J. Vac. Sci. Technol. B* 1991, *9*, 3612. (b) D. J. Keller, C. Chih-Chung, *Surf. Sci.* 1992, *268*, 333.

[16] (a) P. Grütter, W. Zimmerman-Edling, O. Brodbeck, *Appl. Phys. Lett.* 1992, *60*, 2741. (b) K. L. Westra, A. W. Mitchell, D. J. Thomson, *J. Appl. Phys.* 1993, *74*, 368.

[17] S. N. Magonov, A. Ya. Gorenberg, H.-J. Cantow, *Polym. Bull.* 1992, *28*, 577.

[18] H. Chang, A. J. Bard, *Langmuir* 1991, *7*, 1143.

[19] J. P. Pelz, *Phys. Rev. B* 1991, *43*, 6746.

[20] T. R. Albrecht, H. A. Mizes, J. Nogami, S. Park, C. F. Quate, *Appl. Phys. Lett.* 1994, *64*, 1738.

[21] H. A. Mizes, S.-I. Park, W. A. Harrison, *Phys. Rev. B* 1987, *36*, 4491.

[22] R. J. Colton, S. M. Baker, R. J. Driscoll, M. G. Youngquist, J. D. Baldschwieler, W. J. Kaiser, *J. Vac. Sci. Technol. A* 1988, *6*, 349.

[23] J. Ren, M.-H. Whangbo, S. N. Magonov, unpublished results.